GENERALIZED DIFFRACTION-STACK MIGRATION

by

Ge Zhan

A dissertation submitted to the faculty of
The University of Utah
in partial fulfillment of the requirements for the degree of

Doctor of Philosophy

in

Geophysics

Department of Geology and Geophysics

The University of Utah

December 2012

The University of Utah Graduate School

STATEMENT OF DISSERTATION APPROVAL

This dissertation of **Ge Zhan**

has been approved by the following supervisory committee members:

Gerard T. Schuster	, Chair	**10/31/2012** Date Approved
Richard D. Jarrard	, Member	**10/31/2012** Date Approved
Ronald L. Bruhn	, Member	**10/31/2012** Date Approved
Sergio Chávez-Pérez	, Member	**10/31/2012** Date Approved
Sherif M. Hanafy	, Member	**10/31/2012** Date Approved

and by **D. Kip Solomon**, Chair of

the Department of **Geology and Geophysics**

and by Charles A. Wight, Dean of the Graduate School.

ABSTRACT

I present a new migration algorithm denoted as generalized diffraction-stack migration (GDM). Unlike traditional diffraction-stack migration, it accounts for all arrivals in the wavefield, including two-way primaries and multiple arrivals, and it is not subject to the high-frequency approximation of ray tracing. It is as accurate as reverse-time migration (RTM), but, unlike RTM, filtering and muting can be easily applied to the migration operator to reduce artifacts due to aliasing, and unwanted events such as multiples. Unlike RTM, GDM can be applied to common offset gathers. The main drawback of GDM is that it can be more than an order-of-magnitude more computationally expensive than RTM, and requires much more memory for efficient use. To mitigate some of these disadvantages, I present a multisource least-squares GDM method with phase-encoding.

There are six chapters presented after the introduction. Chapter 2 derives the GDM equation by reformulating the standard RTM equation, and shows how GDM is related to the traditional diffraction-stack migration. Chapter 3 shows how the GDM kernel can be filtered to eliminate coherent noise in the migration image. This precise filtering of the migration operator cannot be done with the standard RTM approach, but it can now be performed with the GDM method. In Chapter 4, I develop an antialiasing filter for GDM. This idea is adapted from the traditional antialiasing strategy for Kirchhoff migration, except GDM antialiasing accounts for both primary and multiple reflection events. This is novel antialiasing filter that can be used for filtering the RTM-like imaging operator. In Chapter 5, I show how to mute or filter the GDM operator to emphasize multiple reflection events. I split the GDM operator into two separate parts, the primary migration operator and the multiple migration operator. By computing the dot-product of the migration operators with the data, followed by an optimal stack of the primary-only image and the multiple-only image, a higher resolution in the migration image can be achieved. An additional benefit is that cross-talk between primary and multiple scattered arrivals, often seen in conventional RTM images, are greatly attenuated. Finally, Chapter 6 presents an efficient implementation of least-squares GDM with supergathers. The supergather consists of a blend of many encoded shot gathers, each one with a unique encoding function

that mitigates crosstalk in the migration image. A unique feature of GDM is that the Green's functions (computed by a finite-difference solution to the wave equation) can be reused at each iteration. Unlike conventional least-squares RTM, no new finite-difference simulations are needed to get the updated migration image. This can result in almost two orders-of-magnitude reduction in cost for iterative least-squares migration. Furthermore, when the least-squares GDM is combined with phase-encoded multisource technology, the cost savings are even greater. This is a subject that is discussed in Chapter 7.

The main challenge with GDM is that it demands much more memory and I/O cost than standard RTM algorithm. As a partial remedy, Appendix A describes how to efficiently compute the migration operators either in a target-oriented mode or by using wave equation wavefront modeling. In addition, the intensive I/O and storage costs can be partly, not fully, mitigated by applying a wavelet transform with compression, where a compression ratio of at least an order-of-magnitude can be achieved with a small loss of accuracy. This topic is addressed in Appendix B.

To my wife Minyu.

CONTENTS

LIST OF FIGURES

ACKNOWLEDGMENTS

My PhD studies at the University of Utah since Fall 2007 have been enriched by the great help of many people. Here, I would like to take this honorable opportunity to thank the people who have in no small way made this dissertation available.

First and foremost, I would like to thank my advisor, Prof. Gerard T. Schuster, for all the exciting moments I shared with him in our UTAM and CSIM group. I have profoundly benefited from my association with him over the past 5 years. Without his guidance, supervision and support, I could not survive as a geophysicist without enough knowledge about seismic. I can only hope that, during the past several years, I have been able to absorb some of his magical intuition and endless enthusiasm for researching interesting geophysics. I am also fortunate to have Dr. Richard D. Jarrard, Dr. Ronald L. Bruhn, Dr. Sergio Chávez-Pérez, and Dr. Sherif M. Hanafy as my supervisory committee members. This dissertation was made possible due to the masterly guidance of all my committee members. I truly acknowledge the valuable time, patience, support of my supervisory team.

The strong sense of community within the UTAM group has been an important part of my time at UU. I would like to express my appreciation to all of the group members. In the summer of 2007, I was welcomed by my dear friend Shengdong Liu upon my arrival. And from the very beginning, other colleagues Chaiwoot Boonyasiriwat, Naoshi Aoki, Samuel Brown, Sherif Hanafy, Shuqian Dong, Weiping Cao, Xiang Xiao, and Yanwei Xue helped me a lot to affiliate myself into the group. Shortly after a year, the group's legacy carried on with a new set of people. Qiong Wu, Simin Huang, Wei Dai and Xin Wang joined the group, we shared a great year both at work and in life. I am also very much grateful to Dr. Huilian Ma outside the group for her kind assistance with my daily life in Salt Lake.

In the Summer of 2010, I started the first internship of my life at TGS-NOPEC Geophysical Company in Houston, TX. Because of that, I was given a chance to go to the "real" world and gain valuable industry experience. I owe my deepest gratitude to Dr. James Cai for bringing me there. As my internship mentor, his advice and encouragement were always important guiding lights towards my personal and professional development. The numerous discussions with Shuqian Dong at TGS during that summer helped me to

fulfill my internship project. I thank him for his patience and for the great colleagueship we shared over the years.

During the summer of 2011, I worked with my company mentor, Dr. Brian Hornby at BP America. He not only taught me the state-of-the-art VSP technology, but also broadened my narrow views of geophysical science and society. Although this internship was only three months short, many inspirations from this internship led to the success of my later research. I would also like to emphasize the signicance of my colleagues Dr. Mark Roberts, Dr. Jianhua Yu, Dr. Min Zhou and Dr. Zhiyong Jiang's role during my internship at BP. They continuously supported both my research and personal life when I was there. I had a fruitful summer and I would like to express my appreciation to them.

Finally, I come to the most personal source of gratitude. When my wife Minyu decided to quit her job in Beijing to join me in Salt Lake in 2008, and then to follow me to Jeddah, Saudi Arabia in 2009, she surely never anticipated the frustration and loneliness that has accompanied her sometimes. I thank her for giving me wholehearted love and her sacrifice during my studies. She has been my enduring source of strength and happiness during challenging times. It is her to whom I dedicate this dissertation.

CHAPTER 1

INTRODUCTION

1.1 Motivation

Seismic migration is a method for relocating recorded reflections to their place of origin in the earth. This birthplace is at layer interfaces where there is a contrast in rock impedance, and is imaged as the reflectivity distribution by migration for complex structures such as faults and salt bodies.

The diffraction-stack (Kirchhoff) migration method is widely used in industry for depth imaging. For migrating a single event on a single trace, it smears the event energy to all possible subsurface reflection points in the model space. After smearing and summation of all samples on all traces into the earth model, a diffraction-stack migration image is obtained. This migration method is computationally inexpensive, easily adaptable to different filtering strategies such as obliquity factors, first-arrival restrictions, angle-dependent truncation of data aperture, and antialiasing filters. However, it is subject to the high-frequency approximation of ray tracing, and therefore it has difficulty in complex velocity models which preclude the accurate use of ray tracing or the modeling of multiple scattered arrivals.

As a more accurate alternative, the reverse-time migration (RTM) method is a well established imaging method that uses finite-difference solutions to the wave equation to accurately propagate seismic energy through complex models. The key benefits of RTM compared to diffraction-stack migration method are that, if the velocity model is accurate enough, it can correctly image any dipping structure, can account for multiple arrivals, and has the capability of providing much higher resolution in the reflectivity image. But the price we pay is a computationally expensive algorithm that appears inflexible to efficiency improvements, or operator filtering strategies used in diffraction-stack migration.

To overcome the inability to filter unwanted noise in the RTM operator, I reformulate the equation of reverse-time migration into that of generalized diffraction-stack migration (GDM), where GDM is interpreted as summing data along a series of hyperbola-like curves, each one representing a different type of event such as a reflection or multiple. This is

a generalization of the familiar diffraction-stack algorithm where the migration image at a point is computed by the sum of trace amplitudes along an appropriate hyperbola-like curve. Instead of summing along the curve associated with the primary reflection, the sum is over all scattering events and so this method is named generalized diffraction-stack migration (GDM). The GDM formulation is equivalent to RTM but it leads to filters that can be applied to the GDM operator to mitigate migration artifacts due to aliasing, crosstalk, and multiples.

1.2 Technical Contributions

This dissertation makes several significant contributions to the field of seismic migration and imaging. The core contributions of my dissertation arise from the reformulation of the standard reverse-time migration (RTM) equation as the generalized diffraction-stack migration (GDM) equation. Using the GDM equation, I successfully decompose the kernel of the RTM imaging operator into products of incoming and outgoing Green's functions, which not only gives rise to a deeper understanding of the properties of different kernel components but also leads to an imaging algorithm with less coherent noise and a higher-quality migration image. A second contribution is that, based on the GDM algorithm, an antialiasing filter is developed for RTM. It is similar to the traditional antialiasing filter used for Kirchhoff migration but now provides RTM-like images mostly free of aliasing artifacts. A third contribution is the separation of the GDM operator into primary and multiple reflection components. Consequently, a migration image with a higher resolution is achieved by the use of multiple scattering. These contributions are validated by implementations of the GDM algorithm on both synthetic and field data. A fourth contribution is the development of a phase-encoded least-squares GDM algorithm. The benefit is an increased image resolution, better signal-to-noise ratio of the migration image, and an order-of-magnitude increase in computational efficiency compared to standard least-squares GDM. Finally, I show how the storage costs of GDM can be decreased by using a wavelet-transform compression scheme.

CHAPTER 2

GENERALIZED DIFFRACTION-STACK MIGRATION: A MODIFIED FORM OF REVERSE-TIME MIGRATION

The two end members of migration algorithms are diffraction-stack migration and reverse-time migration (RTM). The former is computationally inexpensive, flexible, but subject to the high-frequency approximation of ray tracing. Consequently, it has difficulty with complex velocity models that preclude the accurate use of ray tracing. To overcome this limitation, reverse-time migration uses finite-difference solutions to the wave equation to accurately propagate seismic energy through complex models. But the price we pay is a computationally expensive algorithm that appears inflexible to efficiency improvements or algorithmic tricks that suppress migration noise such as obliquity and intrinsic antialiasing filters. In this chapter, I will first overview these two migration algorithms and then reformulate the equations of reverse-time migration, so that they can be reinterpreted as a generalized diffraction-stack migration algorithm, which can partly remediate these deficiencies of RTM.

2.1 Theory of Diffraction-stack Migration

A prestack migration image $m(\mathbf{x})$ for a common shot gather (CSG) can be computed with the diffraction-stack migration formula in the frequency domain

$$m(\mathbf{x}) \;=\; \sum_{\omega}\sum_{r} \alpha(\omega,\mathbf{x},\mathbf{r},\mathbf{s})\; \overbrace{[G(\mathbf{x}|\mathbf{s})^{*}G(\mathbf{r}|\mathbf{x})^{*}]}^{migration\ kernel}\; \overbrace{D(\mathbf{r}|\mathbf{s})}^{CSG}, \tag{2.1}$$

where $D(\mathbf{r}|\mathbf{s})$ is the CSG in the frequency domain for a shot at $\mathbf{s}$ and receiver at $\mathbf{r}$, $G(\mathbf{x}|\mathbf{s})$ is the background Green's function which is a solution to the acoustic Helmholtz equation for a source at $\mathbf{s}$ and observed at $\mathbf{x}$, and $m(\mathbf{x})$ is the migration image at the trial image point $\mathbf{x}$. Here, the $G(\mathbf{x}|\mathbf{x}')$ ($\mathbf{x}'$ may be at $\mathbf{s}$ or $\mathbf{r}$) and $D(\mathbf{r}|\mathbf{s})$ spectra depend on angular frequency ω, but its notation is silent. The preconditioning function $\alpha(\omega,\mathbf{x},\mathbf{r},\mathbf{s})$ is defined by the

user, and can compensate for the bandlimited source wavelet, obliquity factor, acquisition footprint, and geometrical spreading.

If $G(\mathbf{x}|\mathbf{x}')$ is the asymptotic Green's function computed by ray tracing and only accounts for single scattering events, then equation 2.1 is the general formula for diffraction-stack migration, which is also known as Kirchhoff migration (KM). The KM point scatterer response of $\sum_\omega \sum_r \alpha(\omega,\mathbf{x},\mathbf{r},\mathbf{s})\ G(\mathbf{x}|\mathbf{s})^* G(\mathbf{r}|\mathbf{x})^* D(\mathbf{r}|\mathbf{s})$ is computed by specifying a trial image point at $\mathbf{x}$ and summing the energy in the CSG along the hyperbola-like red curve in Figure 2.1. This summed energy value is placed at $\mathbf{x}$ and the result is the migration image $m(\mathbf{x})$, and only accounts for primary reflections in the data.

This migration operation can also be interpreted as a dot-product of the kernel fingerprint $G(\mathbf{x}|\mathbf{s})G(\mathbf{r}|\mathbf{x})$ with the CSG fingerprint $D(\mathbf{r}|\mathbf{s})$ (Schuster, 2002), and the result is $m(\mathbf{x})$. If the trial image point is at an actual scatterer, then the fingerprints of the CSG and migration kernel will be a good match and the dot-product will return a large value. If the trial image point is far from any reflector, then the CSG and kernel fingerprints will be mismatched and the dot-product will yield a low magnitude. This description defines the dot-product interpretation of migration, and I will now refer to $G(\mathbf{x}|\mathbf{s})G(\mathbf{r}|\mathbf{x})$ and $D(\mathbf{r}|\mathbf{s})$ as kernel and data fingerprints, respectively.

2.2 Theory of Reverse-time Migration

If $G(\mathbf{x}|\mathbf{x}')$ is computed by a finite-difference solution to the wave equation in the frequency domain, then the equation of prestack reverse-time migration (RTM) can be obtained by right shifting the square brackets in equation 2.1

$$m(\mathbf{x}) \;=\; \sum_\omega \sum_r \alpha(\omega,\mathbf{x},\mathbf{r},\mathbf{s}) \overbrace{G(\mathbf{x}|\mathbf{s})^*}^{forward\ propagate} \overbrace{[G(\mathbf{r}|\mathbf{x})^* D(\mathbf{r}|\mathbf{s})]}^{back\ propagate}. \tag{2.2}$$

The traditional implementation of prestack RTM (Stolt and Benson, 1986) is to back-propagate the data and take the zero-lag correlation of it with the forward propagated source wavefield to get $m(\mathbf{x})$. This is illustrated in Figure 2.2.

2.3 Theory of Generalized Diffraction-stack Migration

In this section, I will first derive the equation for generalized diffraction-stack migration (GDM) and then show how it can be interpreted as a dot-product of the migration kernel with the data.

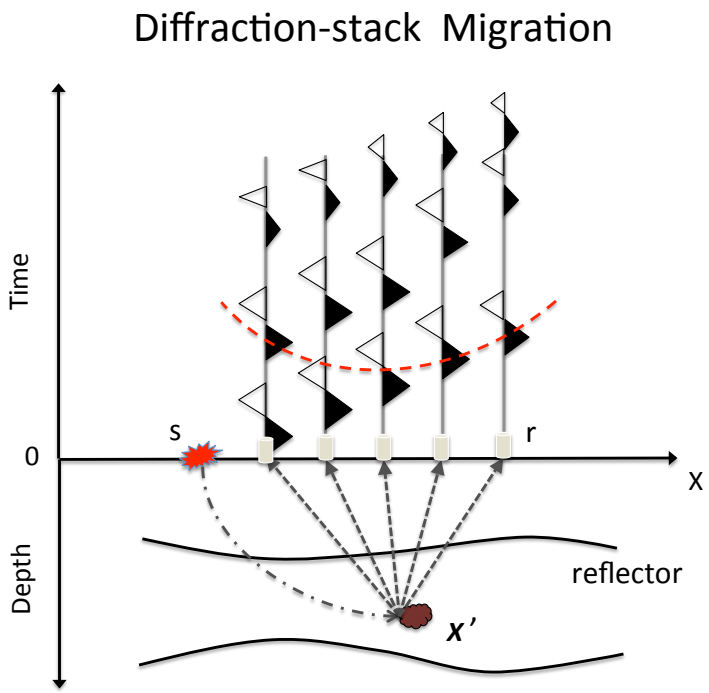

Figure 2.1. Simple diffraction-stack migration operator (red hyperbola) superimposed on the data, which only accounts first arrival scattering information.

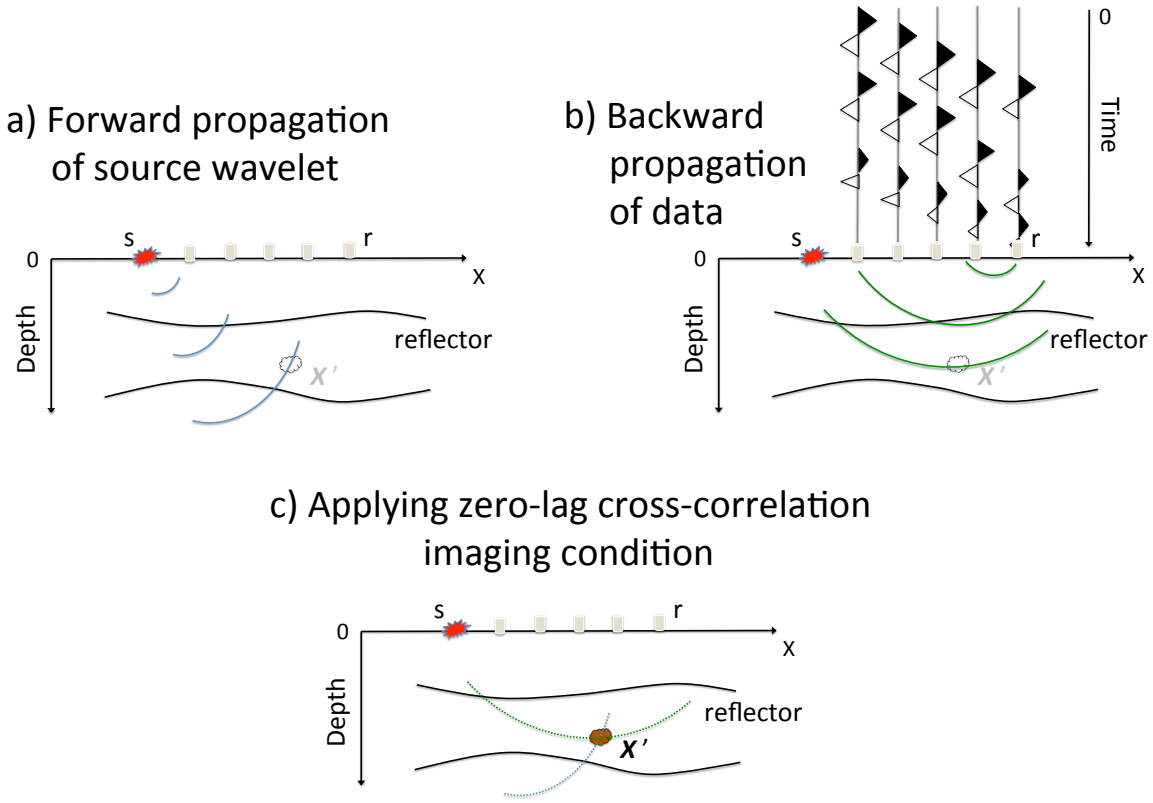

Figure 2.2. The standard reverse-time migration (RTM) image is obtained by computing the zero-lag correlation of the forward-propagated source wavefield a) with the back-projected data b). The scattering point at X' shows up in c) after applying the imaging condition.

For weak scattering, the scattered data $D(\mathbf{r}|\mathbf{s})$ in the frequency domain can be migrated (McMechan, 1983; Stolt and Benson, 1986; Claerbout, 1992) using the Born formula

$$\begin{aligned} m_{mig}(\mathbf{x}) &= \int\int_B \omega^2 G^*(\mathbf{x}|\mathbf{s})\ [G^*(\mathbf{r}|\mathbf{x})D(\mathbf{r}|\mathbf{s})]\ dx_r d\omega, \\ &= \int\int_B g(\mathbf{x},t|\mathbf{s},0)\ [g(\mathbf{r},-t|\mathbf{x},0) * \ddot{d}(\mathbf{r},t|\mathbf{s},0)]\ dx_r dt, \end{aligned} \tag{2.3}$$

where ω is the angular frequency, the frequency integration is over the bandwidth of the source, $G(\mathbf{x}'|\mathbf{x})$ represents the space-frequency Green's function for the Helmholtz equation with a source at $\mathbf{x}$ and a receiver at $\mathbf{x}'$, and $g(\mathbf{x}',t|\mathbf{x},0)$ is the corresponding Green's function in the space-time domain. The term $d(\mathbf{r},t|\mathbf{s},0)$ represents the bandlimited data in the time domain for a source at $\mathbf{s}$ and a receiver at $\mathbf{r}$. Here I have assumed a wideband source spectrum $W(\omega) = 1$ in the Born modeling, the time integration is over the duration time of the trace, and the dx_r integration is over the receiver coordinate $\mathbf{x}_r = (x_r, 0)\ \epsilon\ B$ associated with receivers on a horizontal surface denoted by B.

The double dot symbol represents the trace differentiated twice in time, and $g(\mathbf{r},-t|\mathbf{x},0)*\ddot{d}(\mathbf{r},t|\mathbf{s},0)$ represents convolution of the time reversed Green's function traces with the recorded trace. This operation backpropagates the trace energy at $\mathbf{r}$ to the subsurface at $\mathbf{x}$. In contrast, the Green's function $g(\mathbf{x},t|\mathbf{s},0)$ forward propagates the energy at the source point $\mathbf{s}$ to the subsurface point $\mathbf{x}$, and the migration image at $\mathbf{x}$ is formed by taking the zero-lag temporal correlation of $g(\mathbf{x},t|\mathbf{s},0)$ with the backpropagated trace at $\mathbf{x}$. Traditional reverse-time migration simulates backpropagation by a finite-difference solution to the acoustic wave equation, where the point sources are at the traces located on the surface and the traces act as the time histories for backpropagating seismic wavefields at the receiver locations (McMechan, 1983).

A different implementation of reverse-time migration can be obtained by left shifting the square brackets in equation 2.3 to get

$$\begin{aligned} m_{mig}(\mathbf{x}) &= \int\int_B \omega^2\ [G(\mathbf{x}|\mathbf{s})G(\mathbf{r}|\mathbf{x})]^*\ D(\mathbf{r}|\mathbf{s})\ dx_r d\omega, \\ &= \int\int_B \overbrace{[g(\mathbf{x},t|\mathbf{s},0) * g(\mathbf{r},t|\mathbf{x},0)]}^{GDM\ kernel}\ \ddot{d}(\mathbf{r},t|\mathbf{s},0)\ dx_r dt. \end{aligned} \tag{2.4}$$

The bracketed term

$$\mathcal{G}(\mathbf{r},\mathbf{s},\mathbf{x},t) = g(\mathbf{x},t|\mathbf{s},0) * g(\mathbf{r},t|\mathbf{x},0), \tag{2.5}$$

is the migration kernel that refocuses reflection energy recorded at $\mathbf{r}$ (for a source at $\mathbf{s}$) back to the scatterer at $\mathbf{x}$. As illustrated in Figure 2.3, $\mathcal{G}(\mathbf{r},\mathbf{s},\mathbf{x},t)$ in Figure 2.3a is obtained

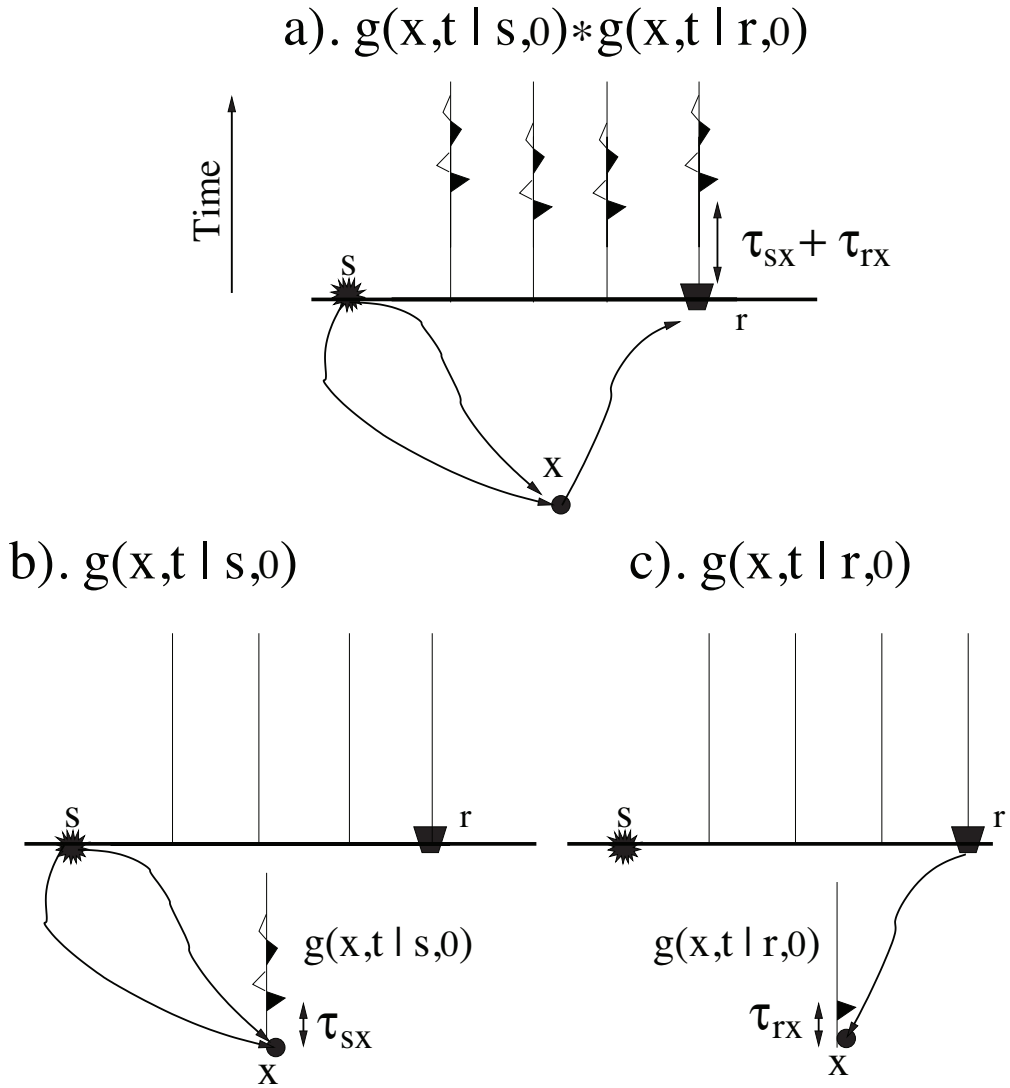

Figure 2.3. Formation of the GDM kernel. a). Migration kernel $\mathcal{G}(\mathbf{r},\mathbf{s},\mathbf{x},t)$ for a fixed image point at $\mathbf{x}$ decomposed into the two modeling kernels: b) one $g(\mathbf{x},t|\mathbf{s},0)$ for a source at $\mathbf{s}$ and the c) other $g(\mathbf{x},t|\mathbf{r},0)$ for a source at $\mathbf{r}$. Convolving the trace in b) with the trace in c) gives the far-right trace shown in a). The other traces in a) represent the migration kernels at other receiver positions.

by computing the Green's function $g(\mathbf{x}', t|\mathbf{x}, 0)$ for a source at $\mathbf{x}$ and receivers at $\mathbf{x}'\epsilon B$, and convolving $g(\mathbf{x}, t|\mathbf{s}, 0)$ in Figure 2.3b with $g(\mathbf{x}, t|\mathbf{r}, 0) = g(\mathbf{r}, t|\mathbf{x}, 0)$ in Figure 2.3c.

Equation 2.4 says that the migration image at $\mathbf{x}$ is computed by taking the dot-product of the shot gather $\ddot{d}(\mathbf{r}, t|\mathbf{s}, 0)$ with the migration kernel $\mathcal{G}(\mathbf{r}, \mathbf{s}, \mathbf{x}, t)$ in Figure 2.3a. This is similar to the interpretation of Kirchhoff migration (KM), except only primary events are accounted for in standard KM, while GDM takes into account both primaries and multiples (Figure 2.4).

2.4 Summary

I have shown that RTM is equivalent to generalized diffraction-stack migration. The generalized migration image at a trial imaging point is obtained by taking the dot-product of the appropriate focusing operator with the data. This is a generalization of simple diffraction-stack migration which sums the data over the appropriate hyperbola.

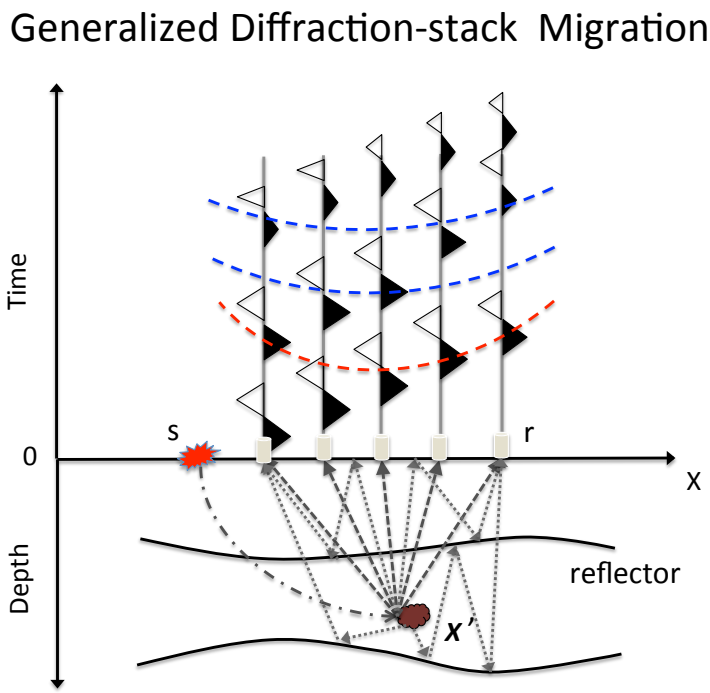

Figure 2.4. Generalized diffraction-stack migration operator (colored hyperbolas) which contains all events in the migration model, including multiples, diffractions and reflections.

CHAPTER 3

FILTERING OF COHERENT NOISE

The standard reverse-time migration (RTM) image is obtained by computing the zero-lag correlation of the back-projected data with the source wavefield. The data are back-projected by a finite-difference algorithm, where each trace acts as a source-time history of a point source at the receiver location. This is a simple and easily understood migration method, but it is not easy to improve by the usual Kirchhoff filters such as obliquity factors, first-arrival restrictions, angle-dependent truncation of data aperture, or antialiasing filters. In Chapter 2, I have reformulated the equation of reverse-time migration so that it can be interpreted as summing data along a series of hyperbola-like curves, each one representing a different type of event such as a reflection or multiple. This formulation leads to filters that can be applied to the generalized diffraction-stack migration (GDM) operator to mitigate coherent migration artifacts due to, e.g., aliasing and crosstalk. Results with both synthetic and field data show that GDM images have less artifacts than those computed by the standard RTM algorithm. The main drawback is that GDM is much more memory intensive and I/O limited than the standard RTM method.

3.1 Introduction

An example of a migration artifact is the strong amplitude, low-frequency noise often seen on RTM images where a high velocity gradient exists. These *crosstalk artifacts* are usually produced by the unwanted cross-correlation of head waves, diving waves and back-scattered waves at the imaging step (Yoon et al., 2004), which severely contaminate the migration image. Various remedies have been proposed to suppress such migration artifacts, such as smoothing the velocity model before migration to reduce reflections (Loewenthal et al., 1987) or low-cut filtering (Mulder and Plessix, 2003) the migration image to reduce artifacts. Fletcher et al. (2005) attenuated reflections at boundaries by introducing a directional damping term to the nonreflection wave equation, while Guitton et al. (2006) reduced artifacts by using a least-squares filter. A physics based migration filter is the

Poynting vector (Yoon and Marfurt, 2006) to improve the cross-correlation based imaging condition. Recently, Liu et al. (2007) and Liu et al. (2011) decomposed the full wavefield of the backpropagated data into their one-way components and applied the imaging condition to the appropriate parts. A similar procedure was used by Fei et al. (2010) where dip filtering was applied to vertical and horizontal slabs of the backpropagated data.

A difficulty with the above approaches is that the precise filtering of the back-projected data cannot distinguish data noise from operator noise. As an example, Kirchhoff migration images can have aliasing artifacts caused by both undersampling the data and the migration operator (Claerbout, 1992). In this case, the data are filtered separately from the migration operator to avoid loss of data information by aggressive filtering. In contrast, the filtered RTM approach of Liu et al. (2011) and Fei et al. (2011) extrapolates the data into the medium and the resulting wavefields are dip filtered at each time step. The back-projected data are hopelessly intertwined with the RTM operator, and so the dip filter simultaneously attacks both data and extrapolator noise. If the noise regime of the operator overlaps the signal of the data, then important data information can be needlessly lost. It is more desirable that the operator is filtered separately from the data.

I now propose a general dip filtering of the reverse-time extrapolation operator that is separate from the data filtering. The operator filtering can be performed using the generalized diffraction-stack migration (GDM) method proposed by Schuster (2002), which is mathematically equivalent to RTM, but its implementation is different. Unlike RTM which intertwines the extrapolation operator with the data at all depth levels, GDM separately computes the complete migration kernel and then applies it to the recorded data in the form of a dot-product to get the migration image. Unlike a Kirchhoff migration (KM) kernel which plots as a single hyperbola-like curve in the shot gather for a specified image point, all events are included in the generalized migration kernel such as direct waves, multiples, reflections, and diffractions. Similar to an antialiasing filter (Lumley et al., 1994) or a dip filter for the KM operator, a filter can be applied to the GDM operator.

This chapter is divided into four parts: an introduction, a theory section that describes the filtering methology, and an application section that applies filters to GDM for both synthetic data and a field data example. The filtering examples are similar to those in Liu et al. (2011) and Fei et al. (2011), except I apply the filter only to the migration kernel to avoid excessive filtering of both data and kernel. The final section is a summary of this work.

3.2 Filtering the GDM Kernel

I will now illustrate dip filtering of the GDM kernel for two simple examples: the horizontal reflector model in Figure 3.1a and the vertical reflector model in Figure 3.1c, each of which has a background velocity that increases with depth. The single trace migration responses are respectively shown in Figures 3.1b and 3.1d, which can be decomposed into separate components with the following analysis.

3.2.1 Horizontal Reflector Model

The Green's function for the horizontal reflector model can be decomposed into downgoing transmitted $D^t(\mathbf{x}|\mathbf{s})$ and upgoing reflected $\mathcal{R}U^r(\mathbf{x}|\mathbf{s})$ wave components in the first layer as illustrated in Figure 3.2:

$$G(\mathbf{x}|\mathbf{s}) = D^t(\mathbf{x}|\mathbf{s}) + \mathcal{R}U^r(\mathbf{x}|\mathbf{s}); \qquad G(\mathbf{x}|\mathbf{r}) = D^t(\mathbf{x}|\mathbf{r}) + \mathcal{R}U^r(\mathbf{x}|\mathbf{r}), \tag{3.1}$$

where $\mathbf{x}$ is the trial image point anywhere along the specular portion of the reflection ray and $\mathcal{R}$ is the reflection coefficient. The superscripts t and r are associated with transmittion and reflection, respectively.

The dominant contributions to the migration image $m_{mig}(\mathbf{x})$ described by equation 2.4 will be along the raypaths where the phase of $G^*(\mathbf{x}|\mathbf{s})G^*(\mathbf{x}|\mathbf{r})$ cancels that for events in the data $\tilde{d}(\mathbf{r}|\mathbf{s}) = \tilde{d^t}(\mathbf{r}|\mathbf{s}) + \tilde{d^r}(\mathbf{r}|\mathbf{s})$, i.e., inserting equation 3.1 into equation 2.4 gives

$$\begin{aligned}
m_{mig}(\mathbf{x}) &= \int\int_B d\omega dx_r\ \omega^2\ [\tilde{d^t}(\mathbf{r}|\mathbf{s}) + \tilde{d^r}(\mathbf{r}|\mathbf{s})]\ [D^t(\mathbf{x}|\mathbf{r}) + U^r(\mathbf{x}|\mathbf{r})]^*\ [D^t(\mathbf{x}|\mathbf{s}) + U^r(\mathbf{x}|\mathbf{s})]^*, \\
&\approx \int\int_B d\omega dx_r\ \omega^2\ [\\
&\quad \overbrace{D^t(\mathbf{x}|\mathbf{r})^* D^t(\mathbf{x}|\mathbf{s})^* \cdot \tilde{d^t}(\mathbf{r}|\mathbf{s})}^{strongest\ trans.\ mig.} \quad \mathbf{x} \in \textit{direct raypath} \\
&\quad + \overbrace{\mathcal{R}^3 U^r(\mathbf{x}|\mathbf{r})^* U^r(\mathbf{x}|\mathbf{s})^* \cdot \tilde{d^r}(\mathbf{r}|\mathbf{s})}^{weakest\ refl.\ mig.} \quad \mathbf{x} \in \textit{specular refl. point} \\
&\quad + \overbrace{\mathcal{R}^2 U^r(\mathbf{x}|\mathbf{r})^* D^t(\mathbf{x}|\mathbf{s})^* \cdot \tilde{d^r}(\mathbf{r}|\mathbf{s})}^{weak\ sou-side\ trans.\ mig.} \quad \mathbf{x} \in \textit{sou-side interbed raypath} \\
&\quad + \overbrace{\mathcal{R}^2 D^t(\mathbf{x}|\mathbf{r})^* U^r(\mathbf{x}|\mathbf{s})^* \cdot \tilde{d^r}(\mathbf{r}|\mathbf{s})}^{weak\ rec-side\ trans.\ mig.} \quad \mathbf{x} \in \textit{rec-side interbed raypath} \\
&\quad + \overbrace{\mathcal{R} D^t(\mathbf{x}|\mathbf{r})^* D^t(\mathbf{x}|\mathbf{s})^* \cdot d^r(\mathbf{r}|\mathbf{s})}^{strong\ refl.\ mig.}\ ] \quad \mathbf{x} \in \textit{specular refl. pt.} + \textit{ellipse},
\end{aligned} \tag{3.2}$$

where unimportant terms are ignored and $\mathbf{x}$ is the trial image point where the phase of the migration kernel is equal and opposite to that of the reflection data.

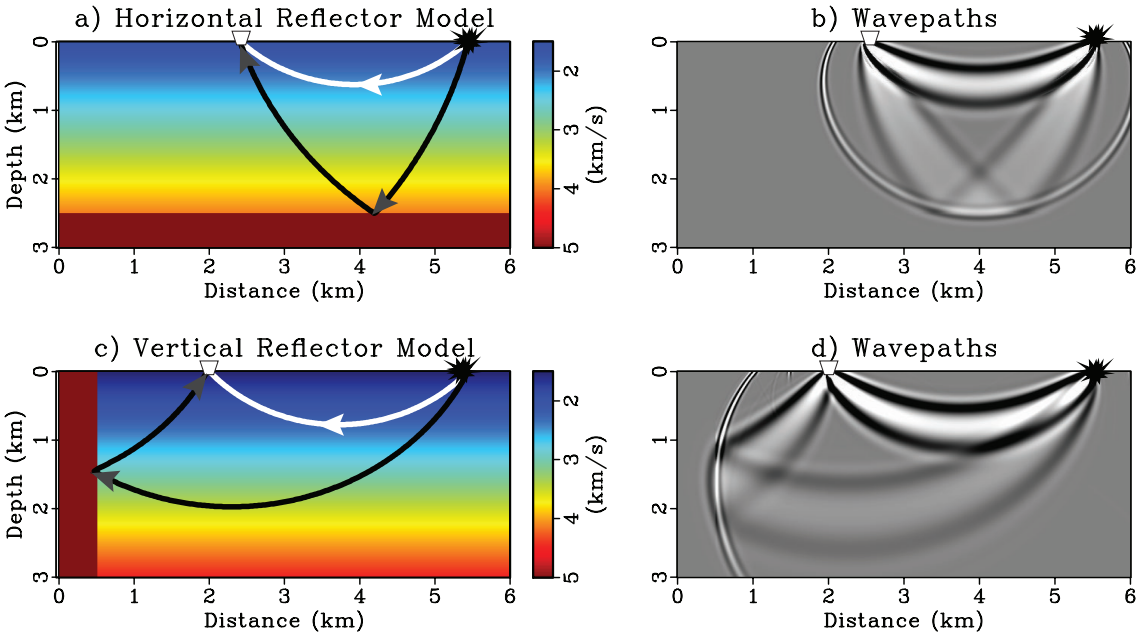

Figure 3.1. Horizontal and vertical reflector models on the left along with their associated wavepaths (Woodward, 1992) to the right. a) shows the horizontal reflector model, and its wavepaths in b) take the shapes of a cigar, rabbit ears, and an elliptical smile. c) and d) are the vertical reflector model and its corresponding wavepaths. The wavepaths were computed by migrating a single trace excited by a wideband point source (star) and recorded at the receiver (quadrilateral).

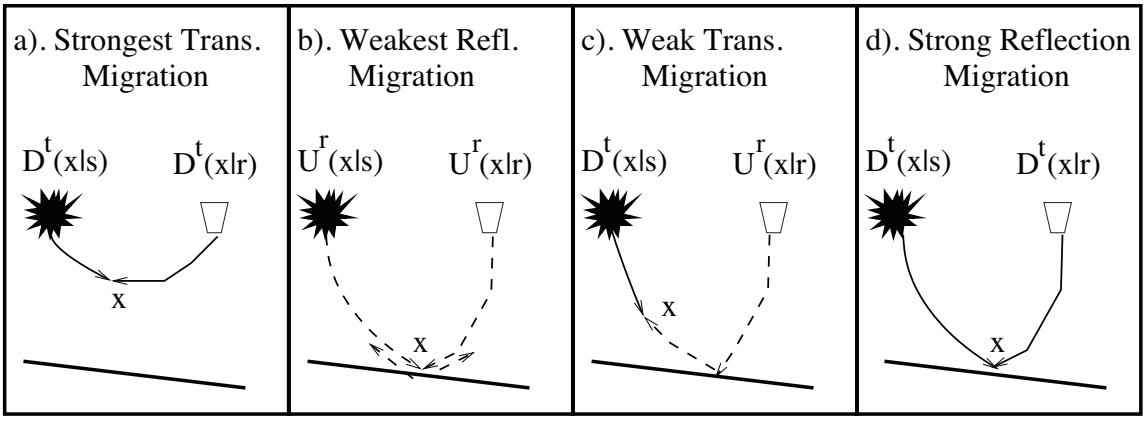

Figure 3.2. Raypaths associated with the products in $[D^t(\mathbf{x}|\mathbf{r}) + U^r(\mathbf{x}|\mathbf{r})]$ $[D^t(\mathbf{x}|\mathbf{s}) + U^r(\mathbf{x}|\mathbf{s})]$. The phase of these products at certain trial image points $\mathbf{x}$ will annihilate the phase in the data for either $\tilde{d}^t(\mathbf{r}|\mathbf{s})$ or $\tilde{d}^r(\mathbf{r}|\mathbf{s})$, but not both. The diving ray in a) can lead to strong artifacts in the RTM image.

The amplitude of the transmitted arrival $\tilde{d}^t(\mathbf{r}|\mathbf{s})$ is $O(1)$, so the strongest part of the migration image $D^t(\mathbf{x}|\mathbf{r})^* D^t(\mathbf{x}|\mathbf{s})^* \tilde{d}^t(\mathbf{r}|\mathbf{s})$ is for $\mathbf{x}$ to be along the direct ray shown in Figure 3.2a, which coincides with the central part of the transmission wavepath in Figure 3.1b. The weakest contribution in the above approximation is $\mathcal{R}^3 U^r(\mathbf{x}|\mathbf{r})^* U^r(\mathbf{x}|\mathbf{s})^* \cdot \tilde{d}^r(\mathbf{r}|\mathbf{s})$ with strength $O(\mathcal{R}^3)$, and contributes at the specular reflection point shown in Figure 3.2b. The undesirable contributions[1] to the migration image are along the interbed raypaths with strength $O(\mathcal{R}^2)$ shown in Figure 3.2c, which coincide with the central portions of the rabbit-ear wavepaths in Figure 3.1b. Finally, the most desirable contribution to the migration image is the Kirchhoff-like image $\mathcal{R} D^t(\mathbf{x}|\mathbf{r})^* D^t(\mathbf{x}|\mathbf{s})^* \cdot d^r(\mathbf{r}|\mathbf{s})$ with strength $O(\mathcal{R})$. It contributes to the image at both the specular reflection point in Figure 3.2d, but also to the thick ellipse in Figure 3.1b.

For reflection migration, only the Kirchhoff-like term should be used and contributions from all other terms should be filtered out. This goal can be accomplished by dip filtering the Green's functions[2] to separate upgoing and downgoing waves, and so only the Kirchhoff-like kernel $D^t(\mathbf{x}|\mathbf{r})^* D^t(\mathbf{x}|\mathbf{s})^*$ should be used for GDM.

As an example, the Green's functions associated with the GDM image in Figure 3.1b can be filtered to give the separate components in Figure 3.3. Here, the desirable image is the ellipse in Figure 3.3a (the last term in equation 3.2), and the undesirable parts are the smile in Figure 3.3b (the 1st term in equation 3.2) and the rabbit ears in Figures 3.3c-d (the 3rd and 4th terms in equation 3.2).

Applying a dip filter to the migration kernels separates the migration image into the different portions shown in Figures 3.3a-d. Since we are only interested in imaging the reflector boundary, then only the migration kernel associated with the ellipse should be used.

3.2.2 Vertical Reflector Model

If the reflector is vertically oriented and the source and receiver are to the right of the reflector, then a dip filter can be used to separate leftgoing and rightgoing terms. Migrating a single trace associated with the vertical reflector model in Figure 3.1c gives the migration image in Figure 3.1d. Only the ellipse-like feature is desired, which can be isolated by

---

[1] However, these undesirable contributions for migration are desirable for full waveform inversion (Mora, 1989).

[2] Dip filtering can be performed in the F-K (frequency-wavenumber) domain or by a local slant-stack algorithm.

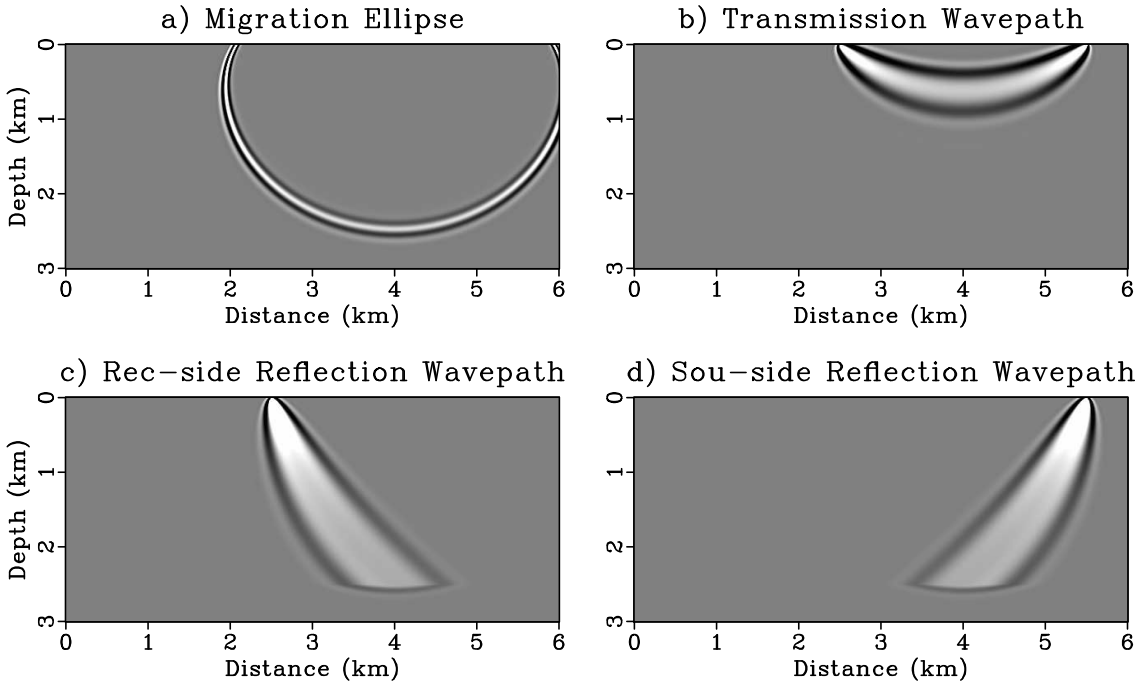

Figure 3.3. Wavepaths in Figure 3.1b separated by dip filtering the migration kernel $G(\mathbf{x}|\mathbf{r})G(\mathbf{x}|\mathbf{s})$ associated with the horizontal reflector model in Figure 3.1a (see the kernels in equation 3.2).

replacing the upgoing reflection Green's function $U(\mathbf{x}|\mathbf{s})$ by the rightgoing one $R(\mathbf{x}|\mathbf{s})$ in equation 3.2 to give

$$
\begin{aligned}
m_{mig}(\mathbf{x}) &= \int\int_B d\omega dx_r\ \omega^2\ [\tilde{d}^t(\mathbf{r}|\mathbf{s}) + \tilde{d}^r(\mathbf{r}|\mathbf{s})]\ [D^t(\mathbf{x}|\mathbf{r}) + R^r(\mathbf{x}|\mathbf{r})]^*\ [D^t(\mathbf{x}|\mathbf{s}) + R^r(\mathbf{x}|\mathbf{s})]^*, \\
&\approx \int\int_B d\omega dx_r\ \omega^2\ [\\
&\qquad \overbrace{D^t(\mathbf{x}|\mathbf{r})^* D^t(\mathbf{x}|\mathbf{s})^* \cdot \tilde{d}^t(\mathbf{r}|\mathbf{s})}^{strongest\ trans.\ mig.} \quad \mathbf{x} \in direct\ raypath \\
&\quad + \overbrace{\mathcal{R}^3 R^r(\mathbf{x}|\mathbf{r})^* R^r(\mathbf{x}|\mathbf{s})^* \cdot \tilde{d}^r(\mathbf{r}|\mathbf{s})}^{weakest\ refl.\ mig.} \quad \mathbf{x} \in specular\ refl.\ point \\
&\quad + \overbrace{\mathcal{R}^2 R^r(\mathbf{x}|\mathbf{r})^* D^t(\mathbf{x}|\mathbf{s})^* \cdot \tilde{d}^r(\mathbf{r}|\mathbf{s})}^{weak\ sou-side\ trans.\ mig.} \quad \mathbf{x} \in sou-side\ interbed\ raypath \\
&\quad + \overbrace{\mathcal{R}^2 D^t(\mathbf{x}|\mathbf{r})^* R^r(\mathbf{x}|\mathbf{s})^* \cdot \tilde{d}^r(\mathbf{r}|\mathbf{s})}^{weak\ rec-side\ trans.\ mig.} \quad \mathbf{x} \in rec-side\ interbed\ raypath \\
&\quad + \overbrace{\mathcal{R} D^t(\mathbf{x}|\mathbf{r})^* D^t(\mathbf{x}|\mathbf{s})^* \cdot d^r(\mathbf{r}|\mathbf{s})}^{strong\ refl.\ mig.} \ ] \quad \mathbf{x} \in specular\ refl.\ pt. + ellipse. \qquad (3.3)
\end{aligned}
$$

Dip filtering can be used to separate the leftgoing and rightgoing waves in the migration kernel, and the image of the desired Kirchhoff kernel is shown in Figure 3.4a. The dot-product of this kernel with the data can be used to get the desirable image of the vertical reflector. Figures 3.4b-d respectively correspond to the 1st, 3rd, and 4th terms in equation 3.3, which are the undesirable parts for migration.

3.3 Numerical Results

3.3.1 Synthetic Data

First, realistic synthetic data are used to illustrate the benefits of filtered GDM to reduce noise in the migration image for imaging the salt-flank model in Figure 3.5. The white lines in Figure 3.5a depict the raypath for a 3rd-order reflection that can significantly contribute to the migration image. Imaging of reflection points at A and C demands the filtering of upgoing and downgoing components for the Kirchhoff-like migration kernel in equation 3.2. In contrast, the migration image at point B requires the filtering of leftgoing and rightgoing events for the last GDM kernel in equation 3.3.

To filter such events, the Green's function for the migration kernel are computed by a finite-difference solution to the wave equation, and Figures 3.6 and 3.7 show the shot gathers recorded along vertical (Figure 3.6b) and horizontal (Figure 3.7b) receiver lines; here the shot is at the surface. These shot gathers are easily dip filtered into their corresponding one-way components, either upgoing (Figure 3.6c) and downgoing (Figure 3.6d) waves for the

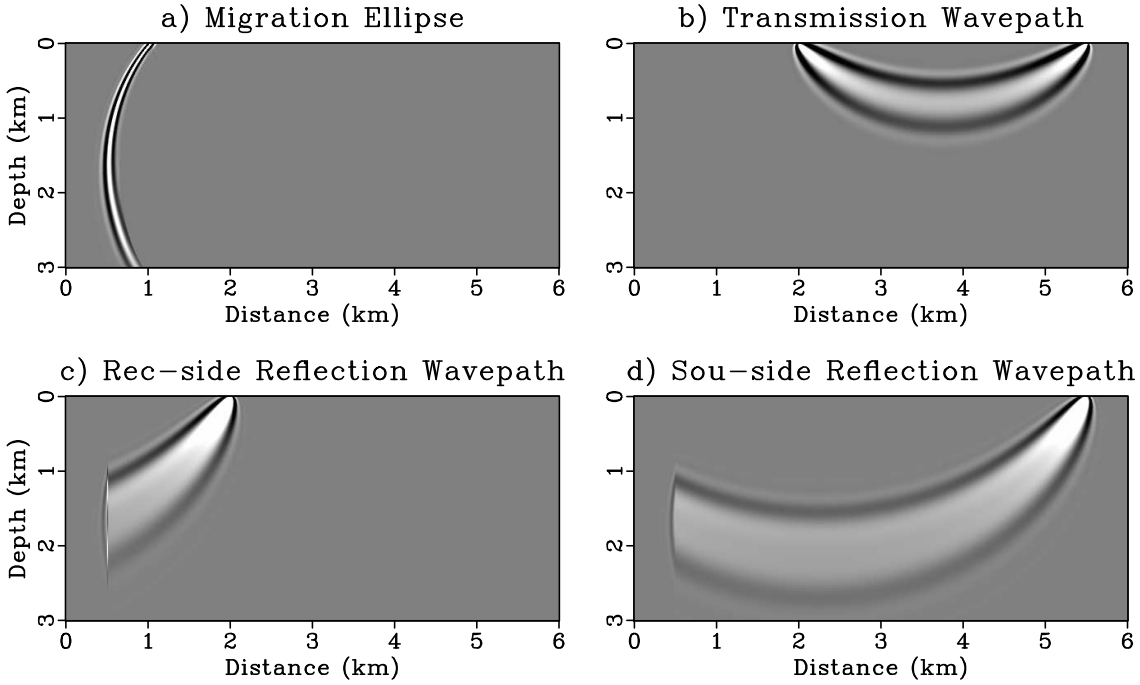

Figure 3.4. Wavepaths in Figure 3.1d separated by dip filtering the migration kernel $G(\mathbf{x}|\mathbf{r})G(\mathbf{x}|\mathbf{s})$ associated with the vertical reflector model in Figure 3.1c.

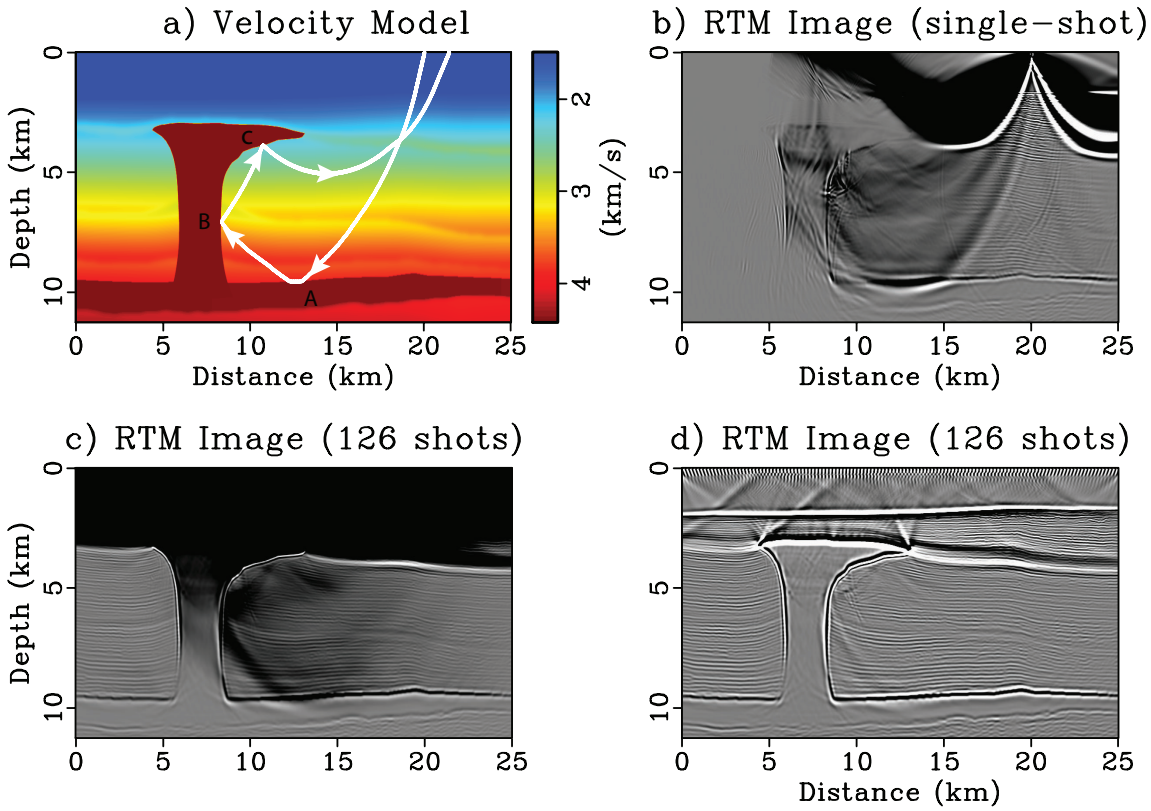

Figure 3.5. RTM results associated with the salt model. a) Salt velocity model overlaid by the raypath of a single source-receiver pair. b), c) and d) are RTM images of this model. Shallow part of the image is overwhelmed by strong artifacts. A high-pass filter is effective in suppressing these artifacts but large residuals still remain.

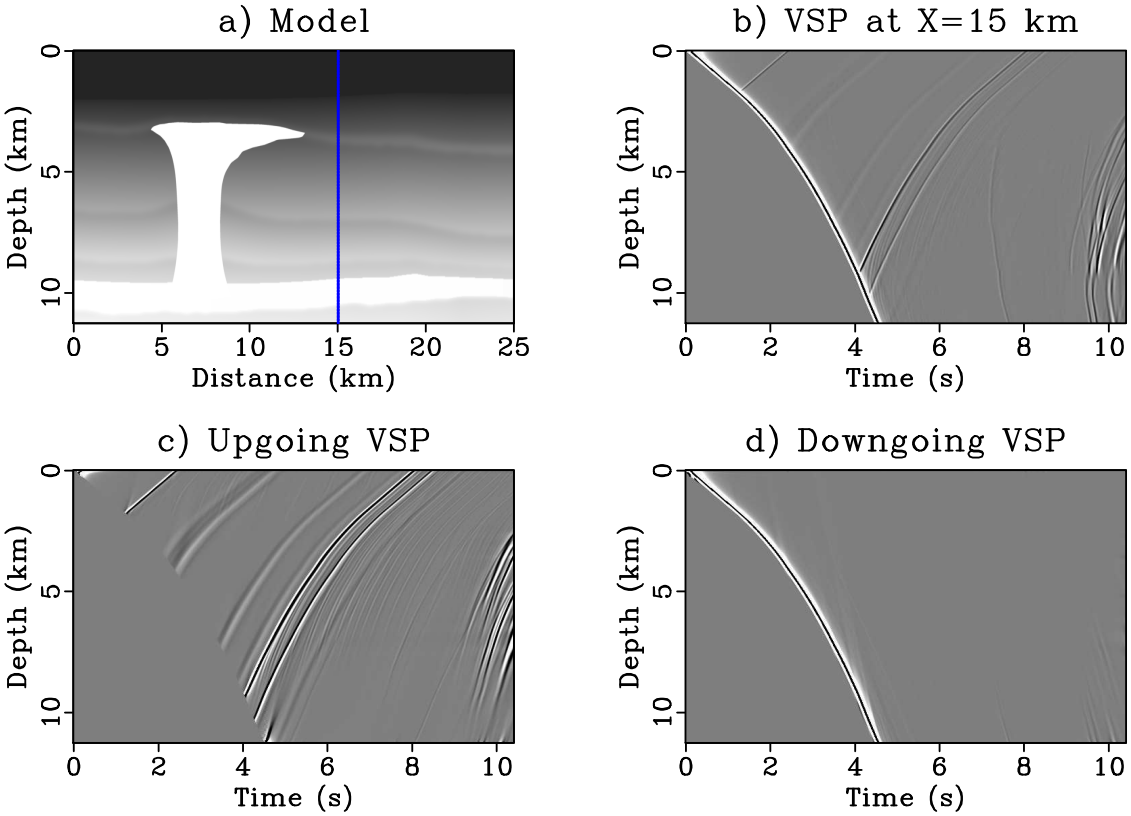

Figure 3.6. Up-down separation of Green's function. a) shows the model. b) is the Green's function recorded along the vertical receiver line. It is then filtered into c) upgoing and d) downgoing components.

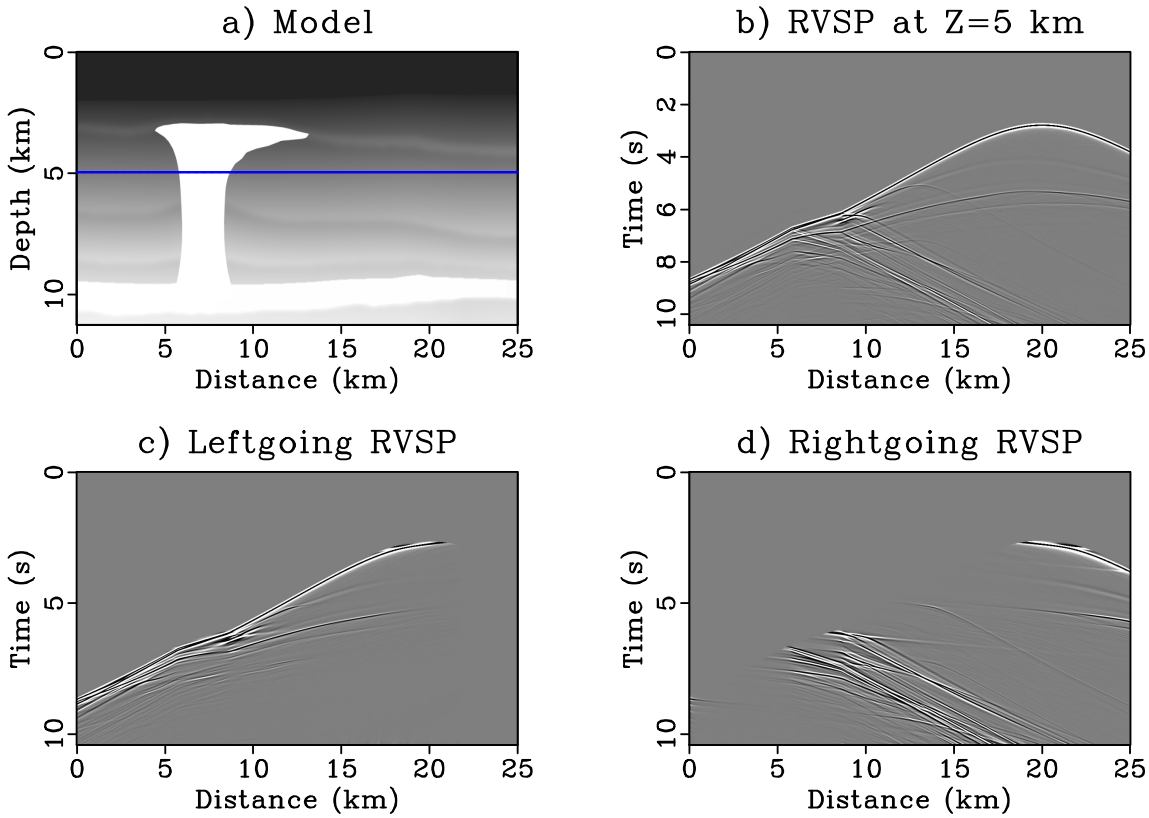

Figure 3.7. Left-right separation of Green's function. a) shows the model. b) is the Green's function recorded along the horizontal receiver line. It is then filtered into c) leftgoing and d) rightgoing components.

vertical line, or leftgoing (Figure 3.7c) and rightgoing (Figure 3.7d) waves for the horizontal line. The Kirchhoff-like kernels in either equation 3.2 or equation 3.3 can then be used to get the, respectively, artifact-free RTM images of a single recorded shot gather in Figures 3.8a and Figures 3.8b. The artifacts are successfully eliminated in Figure 3.8c and the image quality is noticeably improved compared to Figure 3.8d. Figure 3.9 shows a stacked image of 126 such individual single-shot images.

3.3.2 Gulf of Mexico Field Data

Next, I test the filtered GDM on a marine seismic data set recorded in the Gulf of Mexico. This data set is known as the Mississippi Canyon line and was released by Westerngeco as a benchmark test for the 1997 SEG workshop on multiple attenuation (Dragoset, 1999). Figure 3.10a shows the migration velocity model, where a shallow salt body with a high velocity (around 4.7 km/s) is embedded in a background sediment model with a smoothly varying velocity distribution. The water bottom is at a depth of about 1.5 km.

Figure 3.10b displays a raw RTM image migrated with the velocity shown in Figure 3.10a. Due to the strong velocity contrast in the model, especially around the top of the salt, strong amplitude, low-frequency artifacts are present in the image, which are undesired and obscure the image of sediment layers above the salt.

A high-pass filter is applied to this RTM image to reduce these artifacts and the result is shown in Figure 3.11a. As we can see, this simple filtering is effective in reducing the artifacts, but large residuals still remain. To compute an artifact-free image, I apply the filtered GDM algorithm associated with equation 3.2, and only take the last term in equation 3.2 to get the clean image shown in Figure 3.11b. The artifacts are successfully eliminated in Figure 3.11b and as a result, the geology of the shallow sediments is much easier to interpret compared to that in Figure 3.10b.

3.4 Summary

I have shown that RTM is equivalent to GDM, where the generalized migration image at a point $\mathbf{x}$ is obtained by taking the dot-product of the GDM operator with the data. GDM is a generalization of simple diffraction-stack migration which sums the data over the hyperbola-like curve associated with the primary reflections. The advantage of GDM over RTM is that moveout-based noise can be precisely filtered from the migration kernel, which can lead to precise suppression of migration artifacts and avoids unintentional filtering of data. In contrast, the standard RTM approach can only filter the backpropagated data, which is an inseparable mixture of contributions from both the migration kernel

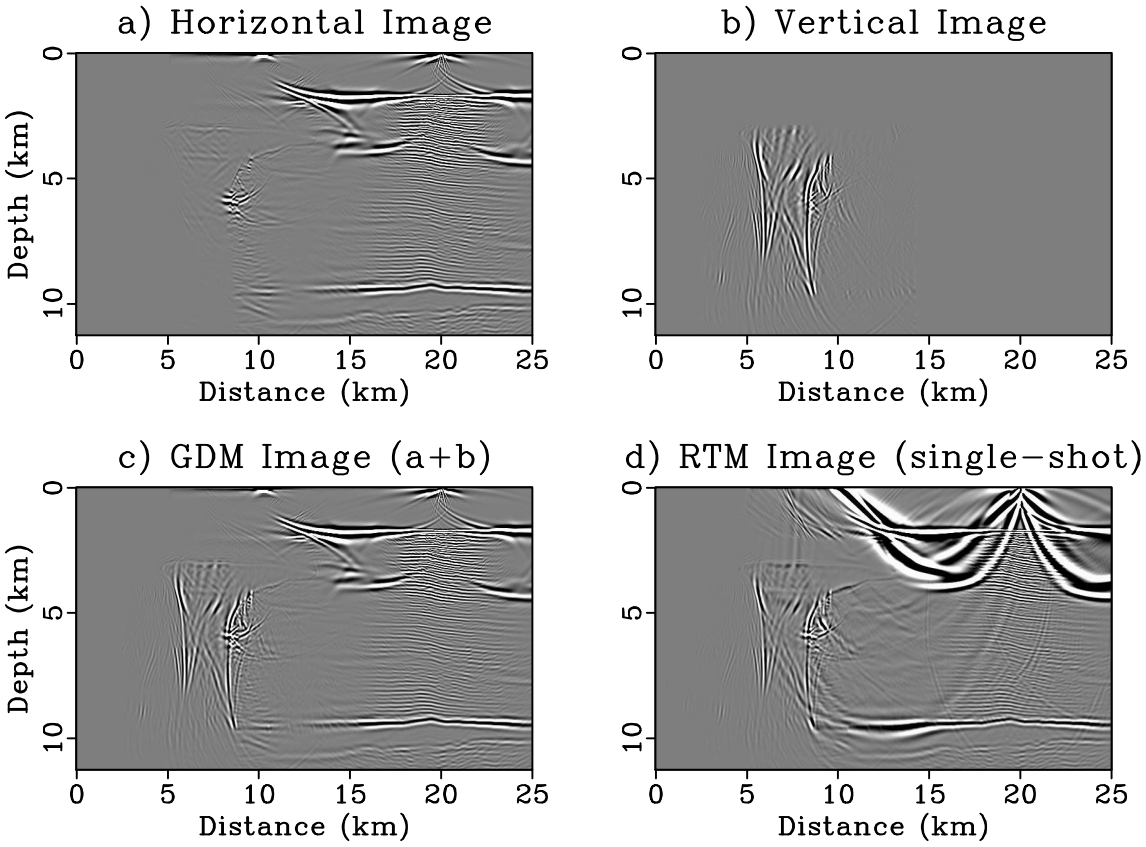

Figure 3.8. Applying the Kirchhoff-like migration kernels in equations 3.2 and 3.3 to recorded data gives, respectively, a) and b). Stacking a) and b) gives c). d) is the standard RTM image.

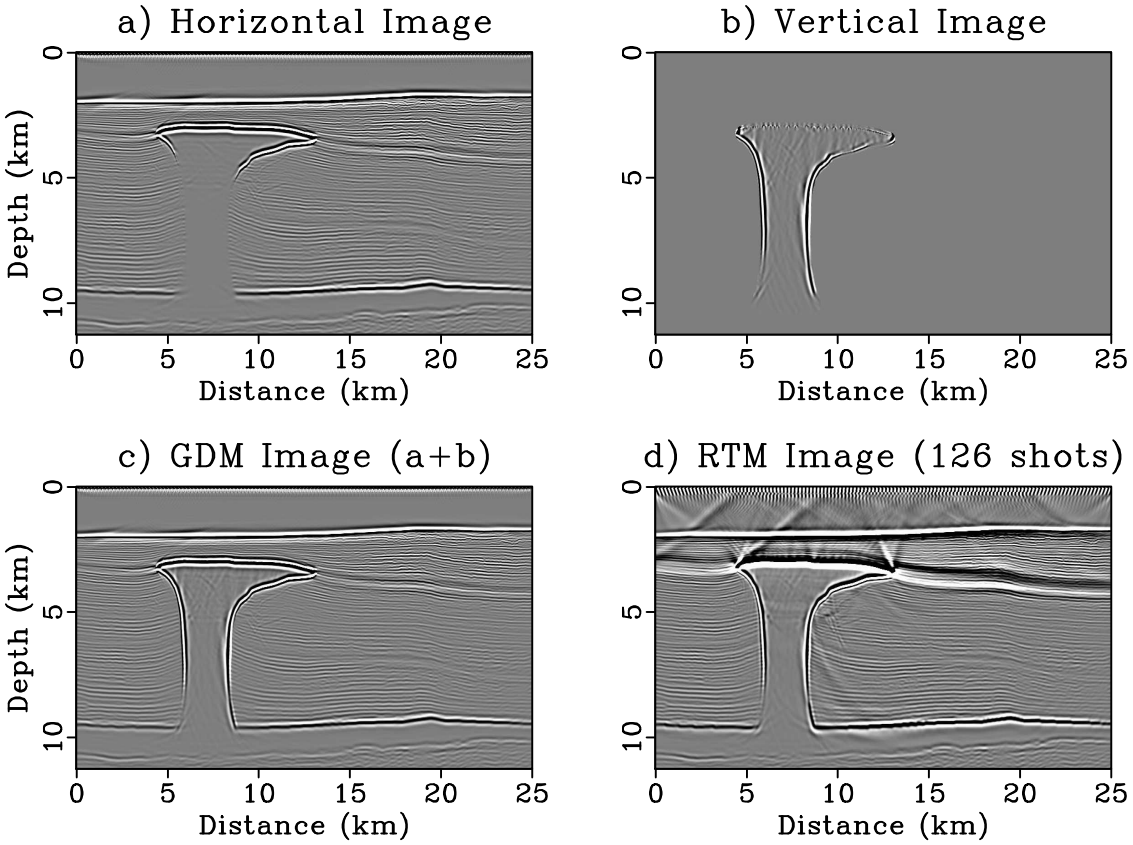

Figure 3.9. Applying the Kirchhoff-like migration kernels in equations 3.2 and 3.3 to all 126 shot gathers gives, respectively, a) and b). c) is the stacking image of a) and b). The high-pass filtered RTM image is shown in d).

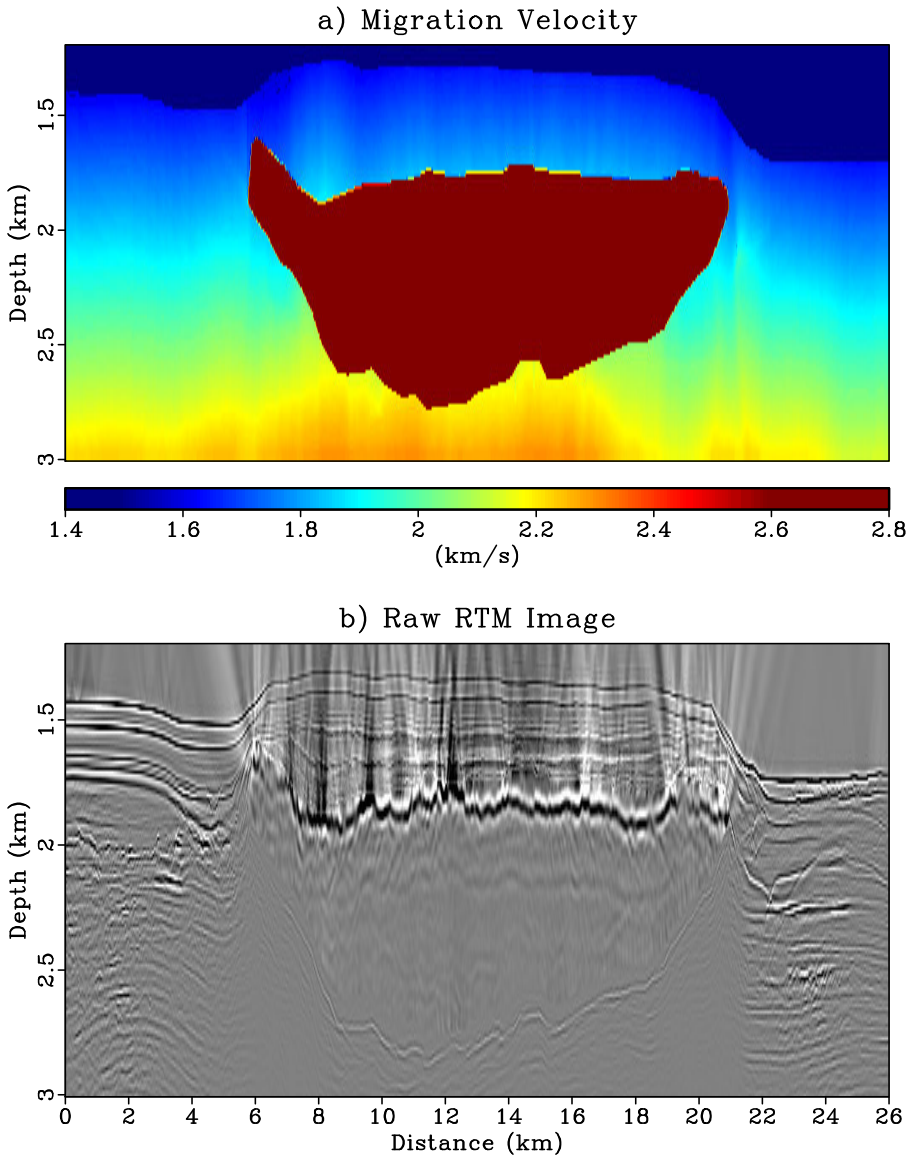

Figure 3.10. The migration velocity and the standard RTM image of the Gulf of Mexico data set.

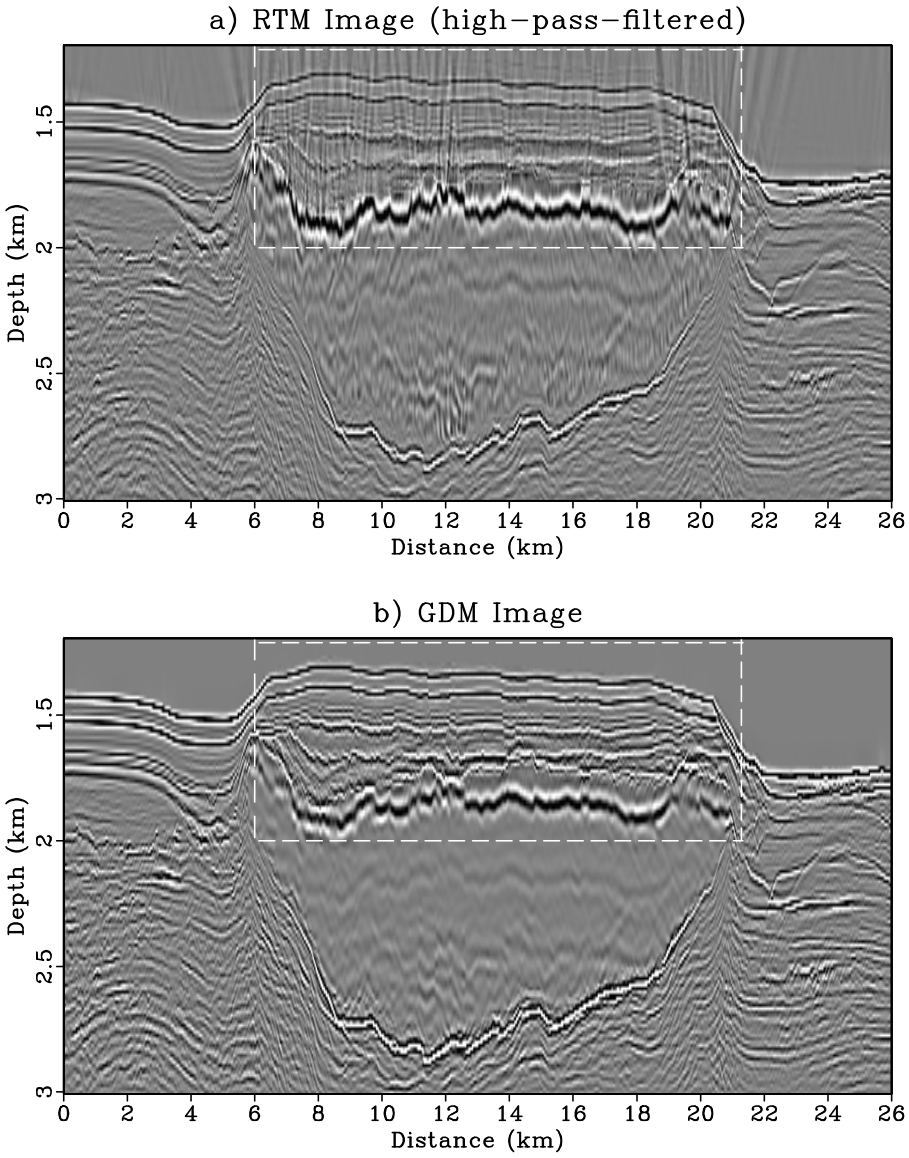

Figure 3.11. The GDM image in comparison with the filtered RTM image. The white dashed box highlights the differences of the two images.

and data. I demonstrated the effective reduction of migration noise by dip filtering the decomposed migration kernel for both realistic synthetic data and field data. Some other useful applications of filtered GDM include mitigation of migration artifacts due to aliasing and multiples (Zhou et al., 2003; Zhou, 2004).

The biggest challenge in implementing GDM is the demanding memory and computation expense of the migration operators. Thus, full blown GDM should be restricted for now to smaller data sets, but with wavelet compression it can be practical for target-oriented migration and iterative least-squares GDM.

CHAPTER 4

ANTIALIASING FILTER FOR MIGRATION

I develop an antialiasing filter for reverse-time migration (RTM). It is similar to the traditional antialiasing filter used for Kirchhoff migration in that it low-pass filters the migration operator so that the dominant wavelength in the operator $\lambda^{oper.}$ is greater than two times the trace sampling interval Δx, except it is applied to both primary and multiple reflection events. Instead of applying this filter to the data in the traditional RTM operation, I apply the antialiasing filter to the generalized diffraction-stack migration operator. This gives the same migration image as computed by antialiased RTM.

4.1 Introduction and Method

A prestack migration image $m(\mathbf{x})$ for a common shot gather (CSG) can be computed with the diffraction-stack migration formula in the frequency domain

$$m(\mathbf{x}) \;=\; \sum_{\omega} \sum_{r} \alpha(\omega, \mathbf{x}, \mathbf{r}, \mathbf{s}) \; \overbrace{[G(\mathbf{r}|\mathbf{x})^* G(\mathbf{x}|\mathbf{s})^*]}^{migration\ kernel} \; \overbrace{D(\mathbf{r}|\mathbf{s})}^{CSG}, \tag{4.1}$$

where $D(\mathbf{r}|\mathbf{s})$ is the CSG in the frequency domain for a shot at $\mathbf{s}$ and receiver at $\mathbf{r}$, $G(\mathbf{x}|\mathbf{s})$ is the background Green's function which is a solution to the acoustic Helmholtz equation for a source at $\mathbf{s}$ and observed at $\mathbf{x}$, and $m(\mathbf{x})$ is the migration image at the trial image point $\mathbf{x}$. Here, the $G(\mathbf{x}|\mathbf{x}')$ ($\mathbf{x}'$ may be at $\mathbf{s}$ or $\mathbf{r}$) and $D(\mathbf{r}|\mathbf{s})$ spectra depend on angular frequency ω, but its notation is silent. The preconditioning function $\alpha(\omega, \mathbf{x}, \mathbf{r}, \mathbf{s})$ is defined by the user, and can compensate for the bandlimited source wavelet, obliquity factor, acquisition footprint, and geometrical spreading.

If $G(\mathbf{x}|\mathbf{x}')$ is the asymptotic Green's function computed by ray tracing and only accounts for single scattering events, then equation 4.1 is the general formula for Kirchhoff migration (KM). The KM point scatterer response of $\sum_{\omega} \sum_{r} \alpha(\omega, \mathbf{x}, \mathbf{r}, \mathbf{s}) \; G(\mathbf{r}|\mathbf{x})^* G(\mathbf{x}|\mathbf{s})^* D(\mathbf{r}|\mathbf{s})$ is computed by specifying a trial image point at $\mathbf{x}$ and summing the energy in the CSG along

the hyperbola-like colored curves in Figure 4.1a. This summed energy value is placed at $\mathbf{x}$ and the result is the migration image $m(\mathbf{x})$, and only accounts for primary reflections in the data.

4.1.1 Migration as Fingerprint Matching

This migration operation can also be interpreted as a dot-product of the kernel fingerprint $G(\mathbf{r}|\mathbf{x})G(\mathbf{x}|\mathbf{s})$ with the CSG fingerprint $D(\mathbf{r}|\mathbf{s})$ (Schuster, 2002), and the result is $m(\mathbf{x})$. If the trial image point is at an actual scatterer, then the fingerprints of the CSG and migration kernel will be a good match and the dot-product will return a large value. If the trial image point is far from any reflector, then the CSG and kernel fingerprints will be mismatched and the dot-product will yield a low magnitude. This description defines the dot-product interpretation of migration, and I will now refer to $G(\mathbf{r}|\mathbf{x})G(\mathbf{x}|\mathbf{s})$ and $D(\mathbf{r}|\mathbf{s})$ as kernel and data fingerprints, respectively.

4.1.2 Antialiasing Filter for Kirchhoff Migration

The antialiasing condition for the KM operator (Gray, 1992; Lumley et al., 1994; Abma et al., 1999; Biondi, 2001; Zhang et al., 2003) says that the local slope dt/dx (e.g., computed from the traveltime table) of the associated hyperbola diffraction curve in $x-t$ space should satisfy the Nyquist sampling criterion:

$$\left|\frac{dt}{dx}\right| \leq \frac{T}{2\Delta x} = \frac{1}{2f\Delta x}, \tag{4.2}$$

where T is the minimum period in the data at frequency f, and Δx is the input trace spacing. If this condition is not satisfied for any (x,t) sample in the CSG, the local portion of this trace at time t is high-cut filtered to $f_{cut} = 1/(2\Delta x)/|dt/dx|$ to eliminate the offending high-frequency components.

4.1.3 Antialiasing Filter for Reverse-time Migration

If $G(\mathbf{x}|\mathbf{x}')$ is computed by a finite-difference solution to the wave equation, then equation 4.1 defines the RTM formula. Its traditional implementation (Stolt and Benson, 1986) is to backpropagate the data and take the zero-lag correlation of it with the forward propagated field to get $m(\mathbf{x})$. An alternative implementation+interpretation of RTM is provided by generalized diffraction-stack migration (GDM). Schuster (2002) showed that the RTM image at $\mathbf{x}$ can be implemented as a dot-product of the kernel fingerprint $\mathcal{F}^{-1}[G(\mathbf{r}|\mathbf{x})G(\mathbf{x}|\mathbf{s})]$ with that of the CSG fingerprint $\mathcal{F}^{-1}[D(\mathbf{r}|\mathbf{s})]$, where $\mathcal{F}^{-1}[\ ]$ represents the inverse Fourier transform. In either the RTM or GDM implementations, the resulting migration images are identical.

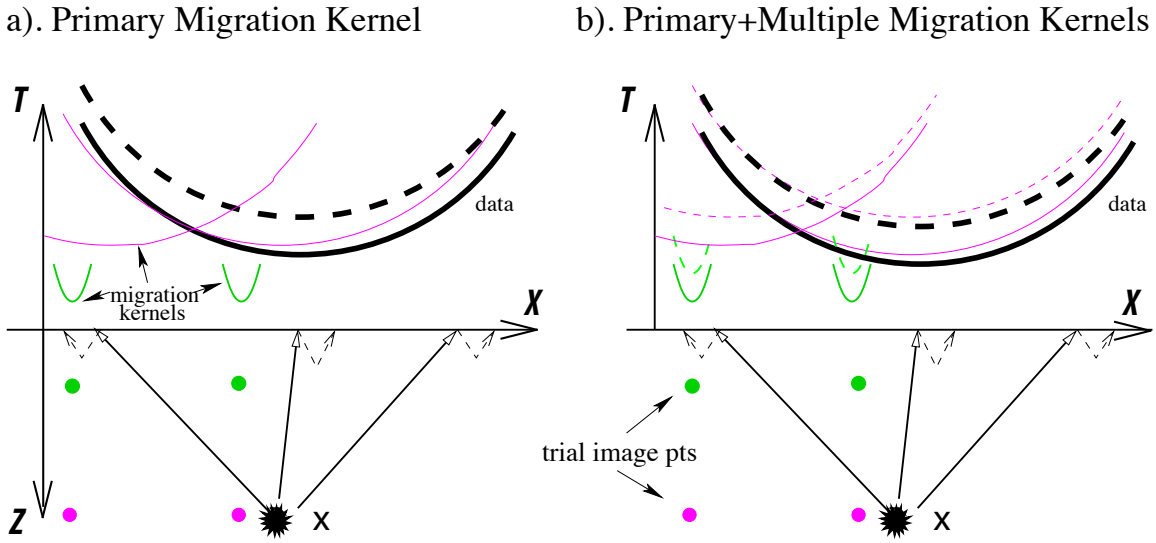

Figure 4.1. Migration kernels plotted in data space as colored hyperbolas for a) primary and b) primary+multiple events associated with shallow (green) and deep (pink) trial image points. The best match between the data (black hyperbolas) and migration curves (pink and green) is when the trial image point is near the actual scatterer's position; the dot-product between the migration kernel and data fingerprints will give the greatest value when the trial image point is at the actual scatterer's location.

As an example, Figure 4.1b shows that the kernel fingerprint consists of several hyperbolas for a specified image point $\mathbf{x}$. The early arriving hyperbola is for the primary scattering and the later one is associated with a multiple. Therefore, the antialiasing strategy for RTM consists of the following:

1. Define $g(\mathbf{r}, t|\mathbf{x}, 0) = \mathcal{F}^{-1}[G(\mathbf{r}|\mathbf{x})]$. Use a finite-difference solution to the space-time wave equation to compute $g(\mathbf{r}, t|\mathbf{x}, 0)$ for a source at $\mathbf{x}$ and receiver at $\mathbf{r}$. Here $\mathbf{x}$ is in the model space.

2. Convolve $g(\mathbf{r}, t|\mathbf{x}, 0)$ with $g(\mathbf{s}, t|\mathbf{x}, 0)$ to get the kernel fingerprint (RTM migration kernel) $\mathcal{G}(\mathbf{r}, \mathbf{s}, \mathbf{x}, t) = g(\mathbf{r}, t|\mathbf{x}, 0) * g(\mathbf{s}, t|\mathbf{x}, 0)$, where $*$ denotes temporal convolution. The convolution results are the colored-line hyperbolas shown in Figure 4.1b.

3. Apply local low-pass filters to every time sample of this kernel so that the antialiasing condition 4.2 is satisfied. Denote this filtered kernel fingerprint as $\tilde{\mathcal{G}}(\mathbf{r}, \mathbf{s}, \mathbf{x}, t)$.

4. Take dot-products of the migration kernel $\tilde{\mathcal{G}}(\mathbf{r}, \mathbf{s}, \mathbf{x}, t)$ with the CSG in the time domain $d(\mathbf{r}, t|\mathbf{s}, 0)$ to get the prestack migration image $m(\mathbf{x})$ for a single shot at $\mathbf{s}$. The resulting image will be free of aliasing artifacts.

4.2 Numerical Results

Synthetic tests associated with a fan model (Figure 4.2a) are presented to demonstrate the effectiveness of the proposed RTM antialiasing filter. The velocity model shown in Figure 4.2a has a homogeneous background velocity of 2000 m/s perturbed by a series of dipping events and deep scatterers with a higher velocity of 2500 m/s. Figure 4.2b displays a typical CSG for this model calculated by a finite-difference (FD) solution to the two-way wave equation. Fifty-one CSGs are computed with the shot interval of 160 m, and the first shot is fired at $X = 2$ km. A fixed spread is used and 301 traces are recorded along the surface with a trace interval of 40 m. The peak frequency of the Ricker wavelet is 15 Hz and the record length is 6 s. Both reflections and diffractions can be clearly seen in the CSG.

Before doing RTM, I first apply the Kirchhoff migration (KM) to this synthetic data set to illustrate the migration aliasing problem for this model. Figure 4.3a shows a CSG with the surface shot at $sx = 7.6$ km, where the direct waves are removed. Figure 4.3b depicts the KM operator, which is a hyperbola for a fixed trial image point at $\mathbf{x}$ (located at $X = 6$ km and $Z = 3$ km). The KM operation for a trial image point $\mathbf{x}$ can be viewed as summing energy along this hyperbola. Figures 4.3c and 4.3d are the corresponding stacked

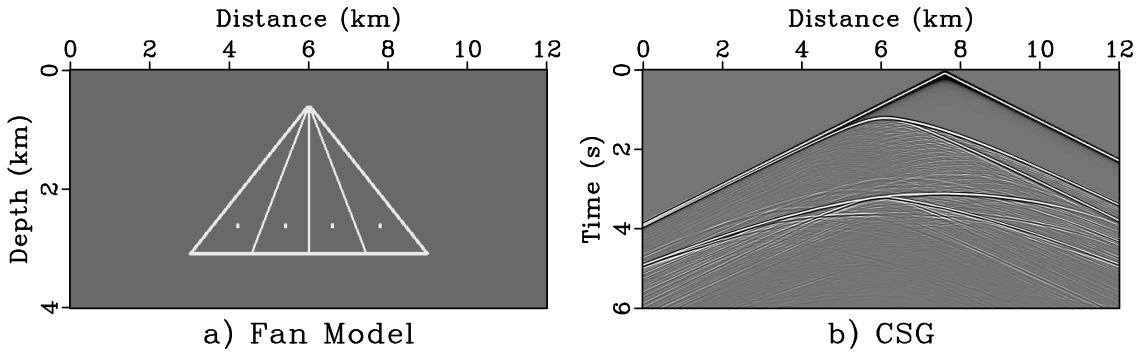

Figure 4.2. Synthetic velocity model and associated shot gather. a) is the fan model, with the background velocity (gray color) of 2000 m/s and the perturbed velocity (white color) of 2500 m/s. b) shows a typical shot gather at $X = 7.6$ km.

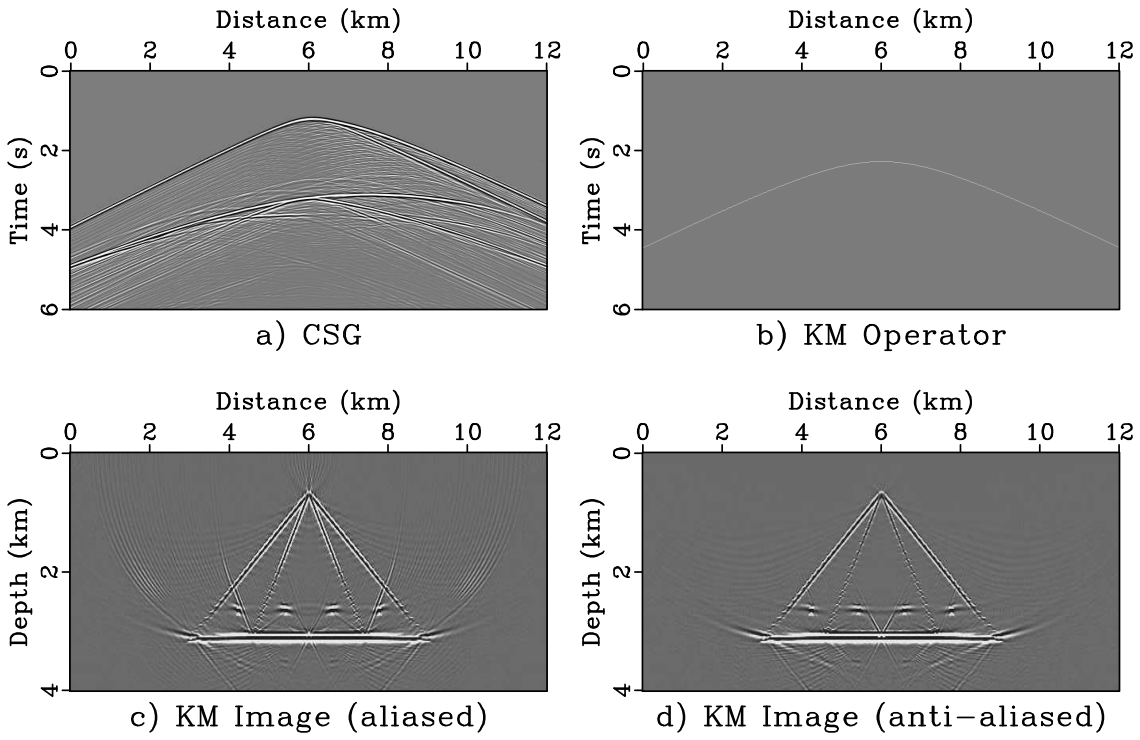

Figure 4.3. Kirchhoff migration (KM) examples.

KM images for 51 CSGs with and without applying an antialiasing filter. Aliasing artifacts are visible in Figure 4.3c and are then suppressed with a KM antialiasing filter proposed by Lumley et al. (1994).

The RTM antialiasing filter described in the theory part is now applied to the same synthetic data. Figure 4.4b presents the RTM operator for the same trial image point and CSG shown in Figure 4.3b. Unlike the hyperbola traveltime curve for the KM operator, the RTM operator contains both primary and multiples along with amplitude and phase information. Figure 4.4c shows the stacked RTM image of this model. Aliasing artifacts seen in the standard RTM image are similar to those in Figure 4.3c. The RTM antialiasing filter is then constructed using the proposed approach and applied to the RTM operator to eliminate the offending high-frequency components. Figure 4.4d displays the RTM image with the antialiasing filtering applied. Compared to Figure 4.4c, the aliasing artifacts are largely eliminated with this filter.

4.3 Summary

I proposed an antialiasing filter for reverse-time migration (RTM). It is similar to the traditional antialiasing filter used for Kirchhoff except that it now accounts for both primary and multiple reflection events. The antialiasing filter is applied to the generalized diffraction-stack migration operator, which gives the same migration image as computed by an antialiased RTM. Numerical results verify the effectiveness of this procedure. The main disadvantage in applying this antialiasing filter is the increased computational cost compared to standard RTM, except in a target-oriented mode. An alternative to antialiased RTM is least-squares migration (LSM) or migration deconvolution (MD). It is observed that LSM (Nemeth et al., 1997) and MD (Yu et al., 2006) appears to overcome aliasing problems and, unlike the traditional antialiasing filter, does not low-pass filter the data. Until recently, LSM was computationally expensive, but Dai et al. (2012) shows that a phase encoded multisource formulation makes it no more expensive than standard RTM. Therefore, MD and LSM might be a viable alternative to an explicit low-pass antialiasing filter applied to the data.

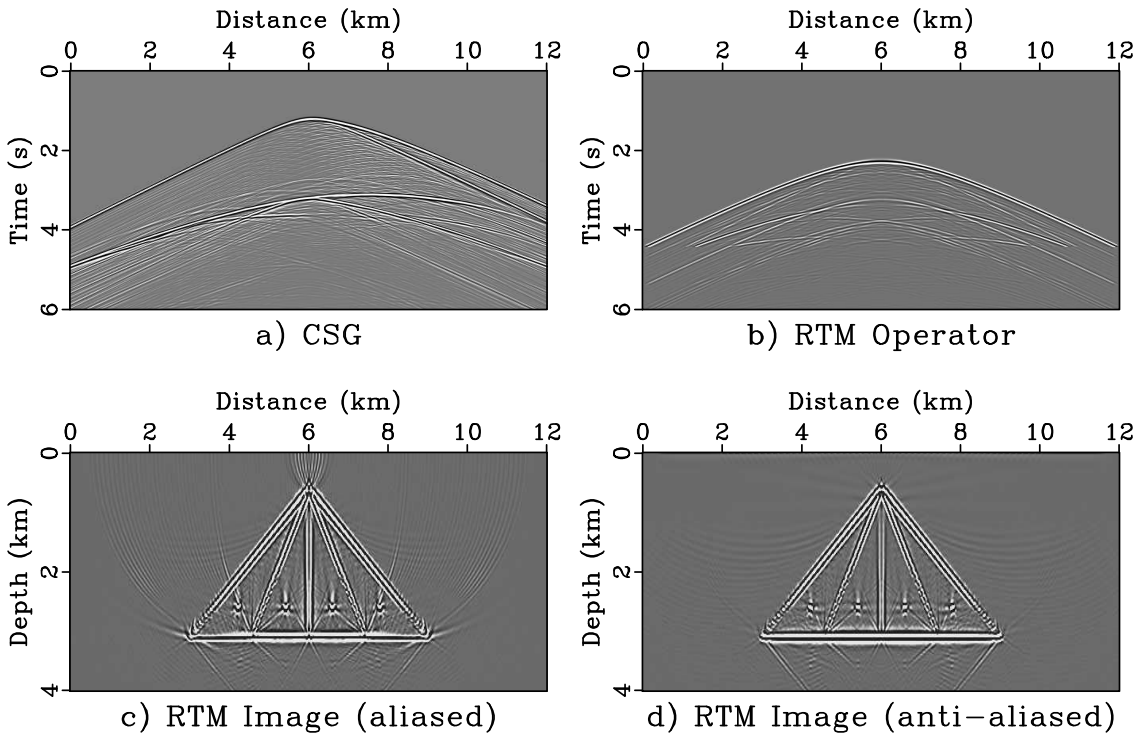

Figure 4.4. Reverse-time migration (RTM) examples.

CHAPTER 5

MIGRATION OF MULTIPLE SCATTERED EVENTS

Recent field tests show the feasibility of achieving superresolution in migration images. To partly realize this with practical exploration data, I introduce a modified form of reverse-time migration, denoted as GDM, with an imaging condition tuned to multiple scattered events. GDM imaging of the SEG/EAGE synthetic data shows higher resolution in the migration image, but at the expense of an increased noise level. A limitation is that superresolution property can be achieved only with a highly accurate velocity model.

5.1 Introduction

The classical limit of spatial resolution in 2D seismic imaging is governed by the range of scattering wavenumber vectors $\boldsymbol{k} = (k_x, k_z)$ in the recorded primary reflection energy. This means that higher frequencies and larger values of k_x lead to better lateral resolution of a point scatterer in a migration image. Equivalently, wider reflection angles and wider source-receiver apertures will lead to better lateral resolution. This idea is quantified by the poststack Rayleigh resolution formula (Elmore and Heald, 1969):

$$\Delta x \quad = 2x = \quad \frac{2\pi z_o}{k(4L)} = \frac{\lambda z_o}{4L}, \tag{5.1}$$

where z_0 is the depth of the point scatterer, L is the aperture width of the poststack traces, k is the wavenumber magnitude, and Δx is the minimum lateral distance between adjacent point scatterers that can just be resolved in a poststack migration image.

To achieve a better horizontal resolution for a fixed aperture width, multiple scattering events should be used. For a complex medium, the multiple scattered energy arrives from a wider range of incidence angles than primaries, and so can yield a much wider range of $\boldsymbol{k}$ values. This enhanced resolution from multiple scattering is now known as superresolution (Blomgren et al., 2002; Lerosey et al., 2007 and many others). Recent studies at the wavelength scale of seismic exploration show that noticeably higher lateral resolution can

be achieved with certain types of field data (Hanafy et al., 2009). For the Hanafy et al. (2009) tests, the field data consist of traces excited by deeply buried seismic sources which is far from the practice of seismic exploration where the sources are near the free surface. The question remains: can superresolution be achieved by migrating seismic data recorded by current technology?

To partly answer this question, I develop a modified form of reverse-time migration (RTM) (Schuster, 2002) and show with synthetic data that it can yield superresolution images if the velocity model is known with high accuracy. However, a drawback is the introduction of noise into the image.

This chapter is divided into three parts: method, examples, and conclusions. I briefly introduce the method first, then I demonstrate synthetic examples on the 2D SEG/EAGE salt model to show the feasibility of superresolution with seismic data. At the end, I draw some conclusions.

5.2 Method

The modified RTM algorithm that emphasizes imaging of multiple scattered events is described as follows.

1. Compute the source-side $g(\mathbf{s},t|\mathbf{x},0)$ and the receiver-side $g(\mathbf{r},t|\mathbf{x},0)$ bandlimited Green's function by a numerical solution to the wave equation, for a source at trial image point $\mathbf{x}$ and the recording position at source position $\mathbf{s}$ and receiver position $\mathbf{r}$, respectively. This assumes an accurate velocity model.

2. Wavelet transform (Luo and Schuster, 1992) the Green's functions $g(\mathbf{s},t|\mathbf{x},0)$ and $g(\mathbf{r},t|\mathbf{x},0)$ to get $\mathcal{W}[g(\mathbf{s},t|\mathbf{x},0)]$ and $\mathcal{W}[g(\mathbf{r},t|\mathbf{x},0)]$, respectively. Then mute all zero values below a given threshold in the wavelet domain and only store those nonzero coefficients to get the compressed Green's functions $\mathcal{W}[\tilde{g}(\mathbf{s},t|\mathbf{x},0)]$ and $\mathcal{W}[\tilde{g}(\mathbf{r},t|\mathbf{x},0)]$. Save these compressed Green's functions on the disk.

3. After reading these compressed Green's functions from disk, an inverse wavelet transform is performed to reconstruct the Green's functions $\tilde{g}(\mathbf{s},t|\mathbf{x},0)$ and $\tilde{g}(\mathbf{r},t|\mathbf{x},0)$ by decompressing $\mathcal{W}[\tilde{g}(\mathbf{s},t|\mathbf{x},0)]$ and $\mathcal{W}[\tilde{g}(\mathbf{r},t|\mathbf{x},0)]$. This is followed by a convolution step to get the compressed migration kernel:

$$\tilde{\mathcal{G}}(\mathbf{r},\mathbf{s},\mathbf{x},t) \quad = \quad \tilde{g}(\mathbf{s},t|\mathbf{x},0) * \tilde{g}(\mathbf{r},t|\mathbf{x},0). \tag{5.2}$$

Here, tilde denotes the function after lossy compression and decompression.

4. The compressed migration kernel $\tilde{\mathcal{G}}(\mathbf{r},\mathbf{s},\mathbf{x},t)$ is a Kirchhoff-like kernel that describes, for a single shot gather, pseudo-hyperbolas of multiarrivals in $\mathbf{r}$-t space. The reflection

energy in a recorded shot gather $d(\mathbf{r},t|\mathbf{s},0)$ is then summed along such pseudo-hyperbolas to give the migration image,

$$m_{mig}(\mathbf{x}) \;=\; \sum_s \sum_r \sum_t \tilde{\mathcal{G}}(\mathbf{r},\mathbf{s},\mathbf{x},t)\; d(\mathbf{r},t|\mathbf{s},0). \tag{5.3}$$

This summation is equivalent to a dot-product between the recorded shot gathers and the compressed migration kernel. It is just like Kirchhoff migration except there is no high-frequency approximation and multiarrivals are included in the imaging (Schuster, 2002); this method will be denoted as generalized diffraction-stack migration (GDM).

5.3 Numerical Results

I tested the GDM method on the 2D SEG/EAGE salt model (see Figure 5.1a) and associated synthetic data computed by FD solutions to the 2D acoustic wave equation. The data include shot gathers generated by 323 shots with a peak-frequency of 13 Hz. There are 176 receivers in each shot gather, and shot and receiver intervals are 48.8 m and 24.4 m, respectively. There are 1001 time samples with a time interval of 0.008 s in each trace. To reduce the computation time, I only focus on the small region below the salt shown in Figure 5.1b.

Figure 5.2a shows a typical Green's function generated by the wave equation solver. I first mute everything but the early-arrivals of the Green's function (Zhou and Schuster, 2002), and the migration kernel is calculated by convolving only the traces with the early-arrivals (Figure 5.2b), which only employs a few periods of the wavefront. The GDM image of the early-arrivals is shown in Figure 5.3a. For comparison, I also implement the GDM using the entire wavefield (Figure 5.2a) instead of just using the early-arrivals. The migration result is shown in Figure 5.3b. The wavefront image (Figure 5.3a) and the entire waveform image (Figure 5.3b) are almost identical. The reason is that the direct waves, or the early-arrivals in the Green's function are the strongest events, the amplitude of which is about two orders-of-magnitude larger than that of the multiples. Therefore, after the dot-product and stacking processes, the contributions of the weak-amplitudes (i.e., later arrivals) of the multiples in the migration image are concealed by the relatively strong-amplitudes of the direct waves and primaries. This can be mathematically demonstrated in the following way.

The Green's function shown in Figure 5.2a can be divided into two parts, direct waves (Figure 5.2b) and multiples (Figure 5.2c):

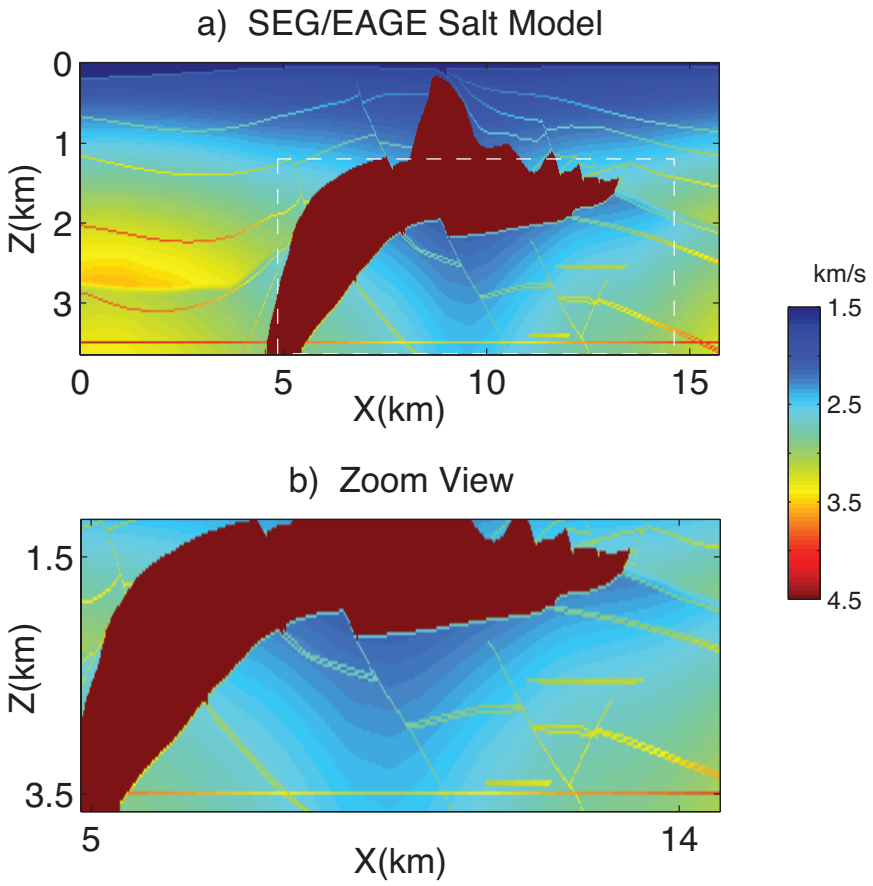

Figure 5.1. Velocity model used in the synthetic tests.

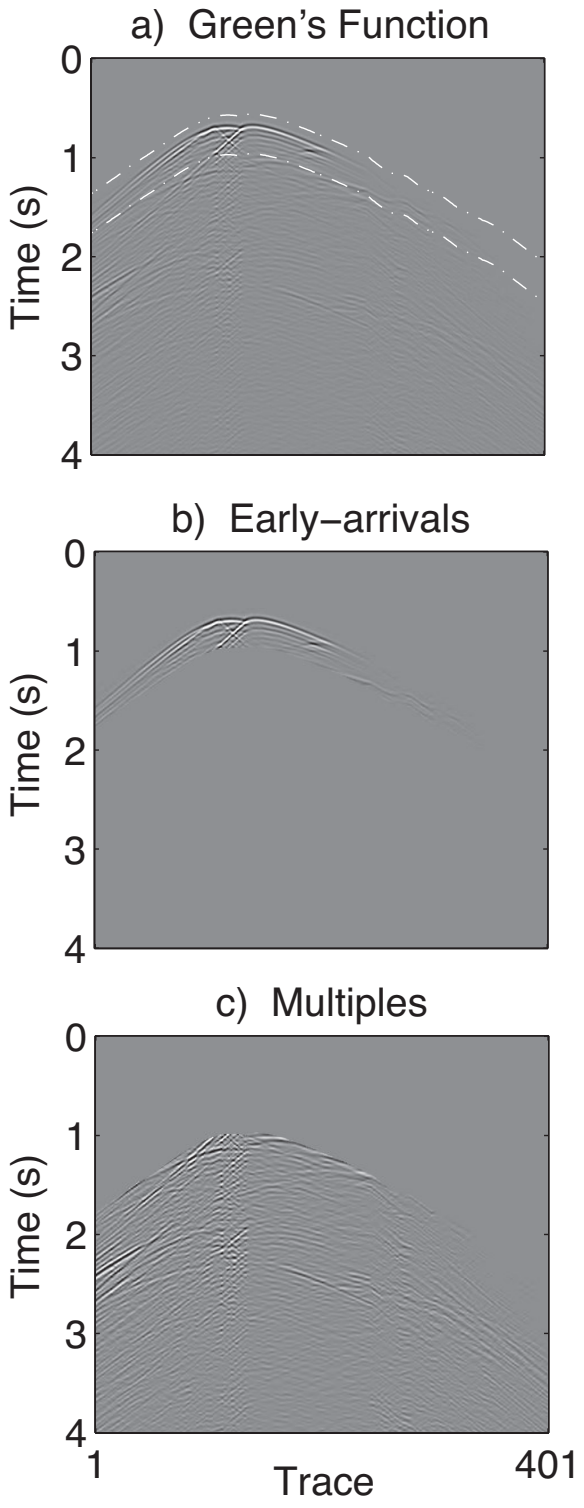

Figure 5.2. Synthetic Green's function and its separation in time. a) A typical bandlimited Green's function generated from the 2D SEG/EAGE salt model. The dashed box shows b) the early-arrivals. c) The Green's function only containing multiples.

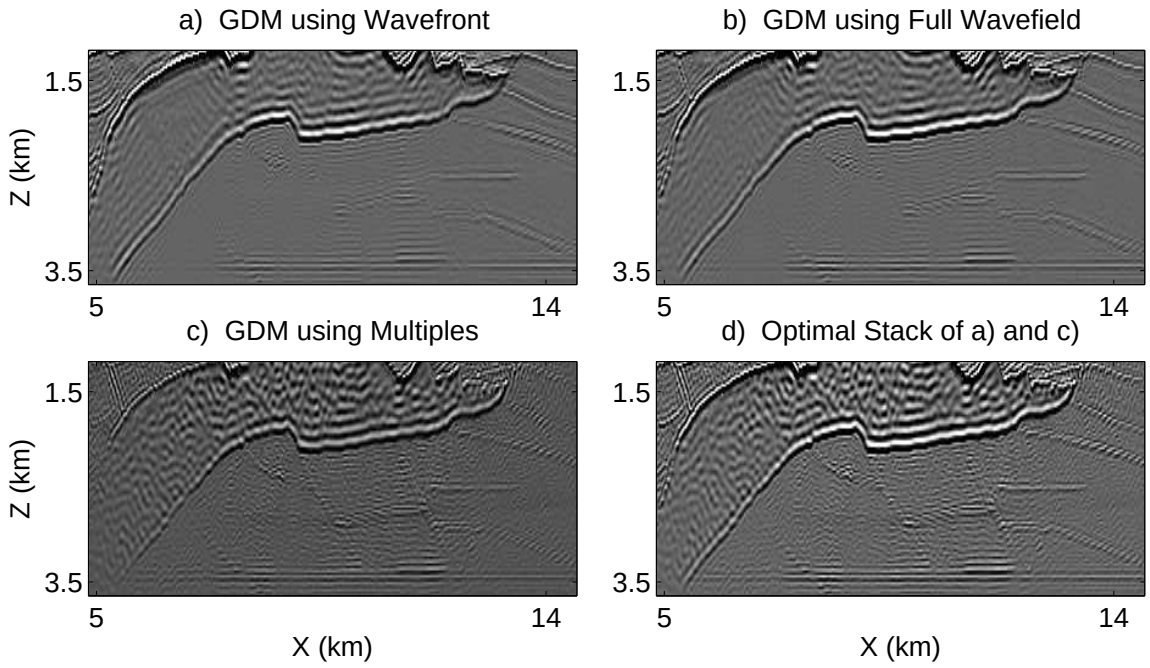

Figure 5.3. Migration results using the GDM method. a) Migration image constructed from migration kernel formed by convolving the early-arrivals. b) Migration image using all of the arrivals to form a migration kernel. c) Migration image using only multiples in the migration kernel. d) The optimal stack of a) and c).

$$\begin{aligned}\tilde{g}(\mathbf{s},t|\mathbf{x},0) &= \tilde{g}_s^D + \tilde{g}_s^M,\\ \tilde{g}(\mathbf{r},t|\mathbf{x},0) &= \tilde{g}_r^D + \tilde{g}_r^M,\end{aligned} \tag{5.4}$$

where the superscripts D and M stand for direct waves and multiples. And the subscripts s and r denote the source-side and receiver-side Green's function, respectively. Plugging equation 5.4 into 5.2, I get

$$\tilde{\mathcal{G}}(\mathbf{r},\mathbf{s},\mathbf{x},t) = \tilde{g}_s^D * \tilde{g}_r^D + \tilde{g}_s^M * \tilde{g}_r^M + \tilde{g}_s^D * \tilde{g}_r^M + \tilde{g}_s^M * \tilde{g}_r^D. \tag{5.5}$$

It is clear that the generalized diffraction-stack migration using the early-arrivals of the Green's function is nothing but the dot-product of the recorded shot gathers with the first term of the migration kernel in equation 5.5. The direct waves are strong compared to multiples, so the other three terms in equation 5.5, especially the second term, is very small compared to the first term. Therefore, when I apply the GDM using the entire wavefield of the Green's function, I get nearly the same result as applying the GDM using early-arrivals only.

Inspired by the above analysis, I calculate the GDM images separately, one using the direct-wave migration kernel and the other using the multiple migration kernel; and then compute the optimal weighting factor before stacking the two images together. Here I only consider the first two parts of equation 5.5 and neglect the last two terms. This is illustrated by rewriting equation 5.3 as

$$\begin{aligned}m_{mig}(\mathbf{x})' &= \sum_s \sum_r \sum_t \left[\tilde{g}_s^D * \tilde{g}_r^D + \beta\left(\tilde{g}_s^M * \tilde{g}_r^M\right)\right] d(\mathbf{r},t|\mathbf{s},0)\\ &= \sum_s \sum_r \sum_t \left(\tilde{g}_s^D * \tilde{g}_r^D\right) d(\mathbf{r},t|\mathbf{s},0)\\ &+ \beta \sum_s \sum_r \sum_t \left(\tilde{g}_s^M * \tilde{g}_r^M\right) d(\mathbf{r},t|\mathbf{s},0),\end{aligned} \tag{5.6}$$

where β is the optimal weighting factor for stacking migration images in a small window. Hence, the contribution from both the direct waves and multiples are equalized which in theory should result in a more detailed migration image.

Figure 5.3c shows the GDM result using the Green's function only containing multiples (Figure 5.2c); this migration kernel is generated by muting the early-arrivals in the dashed box shown in Figure 5.2a and keeping all multiple arrivals. This indeed represents the second term in equation 5.6. Comparing with Figures 5.3a and 5.3b, I get a migration image with better illumination of the subsalt structure and inevitably more noise as well. After estimating the optimal factor β, I stack the two images from the primary reflection

migration (Figure 5.3a) and the migration of multiples (Figure 5.3c) following equation 5.6; and I finally get the optimal stacked image shown in Figure 5.3d. Note that more noise is introduced in Figure 5.3d using this method, but such artifacts can be attenuated with a least-squares migration algorithm.

5.4 Summary

I introduce the theory for compressed generalized diffraction-stack migration that is tuned to migrate multiple scattering events. A wavelet transform is used to compress both source-side and receiver-side Green's functions and a compression ratio of 10 is reached with a small loss of accuracy in the Green's functions. The computation time of the GDM is greatly reduced due to the compression of these Green's functions and a migration image with a higher lateral resolution is achieved by the use of multiple scattering. However, the compression ratio of 10 is still not enough for an efficient implementation of this method. I will assess the feasibility for efficiently implementing both the convolution and the dot-product in the wavelet domain instead of the time domain in the future. An important challenge in achieving superresolution images is how to estimate an accurate migration velocity model so that multiple scattering events can be properly focused.

CHAPTER 6

LEAST-SQUARES WAVE-EQUATION MIGRATION

The theory for skeletonized least-squares wave equation migration (LSM) is presented. The key idea is, for an assumed velocity model, the source-side Green's function and the receiver-side Green's function are computed by a numerical solution of the wave equation. Only the early-arrivals of these Green's functions are saved and skeletonized to form the migration kernel by convolution. Then the migration image is obtained by a dot product between the recorded shot gathers and the migration operator for every trial image point. The key to an efficient implementation of iterative LSM is that at each conjugate gradient iteration, the migration operator is reused and no new finite-difference (FD) simulations are needed to get the updated migration image. It is believed that this procedure combined with phase-encoded multisource technology will allow for the efficient computation of wave equation LSM images in less time than that of conventional reverse-time migration (RTM).

6.1 Introduction

Wave equation migration methods can be very expensive compared to diffraction-stack migration methods. The conventional RTM approach requires a numerical solution to the wave equation for every source position. Hence, much research effort has been spent in reducing the costs of RTM.

I propose to reduce the costs of both standard RTM and least-squares RTM by skeletonizing the migration operator $\mathcal{G}(\mathbf{r},\mathbf{s},\mathbf{x},t) = g(\mathbf{s},t|\mathbf{x},0) * g(\mathbf{r},t|\mathbf{x},0)$ into a skeletonized one $\hat{\mathcal{G}}(\mathbf{r},\mathbf{s},\mathbf{x},t) = \hat{g}(\mathbf{s},t|\mathbf{x},0) * \hat{g}(\mathbf{r},t|\mathbf{x},0)$ with only a few nonzero samples; each sample is at the arrival time of an important early-arrival event (e.g., a primary reflection or a multiple arrival reflection). Thus the onerous storage costs (Zhou and Schuster, 2002; Cao, 2007) of a migration kernel trace with 1001 samples is reduced to a sparse trace with just 10 or so samples. The sparsity of this migration kernel can also reduce migration artifacts by eliminating unnecessary events for high-quality migration images.

Once the skeletonized migration kernel is saved, it does not need to be recomputed at each LSM iteration so this can result in almost two orders-of-magnitude reduction in cost for iterative least-squares migration (Nemeth et al., 1999; Aoki and Schuster, 2009) or waveform inversion. If it is combined with phase-encoded multisource technology (Dai and Schuster, 2009; Krebs et al., 2009), the cost savings can be even greater.

This chapter is divided into three parts: theory, numerical results, and conclusions. I briefly introduce the theory first, followed by the synthetic tests on the 2D SEG/EAGE salt model that demonstrate the effectiveness of this method. At the end, I draw some conclusions.

6.2 Theory

The theory for generalized diffraction-stack migration (GDM) was described by Schuster (2002), who reformulated the equations of RTM so that they can be reinterpreted as a GDM algorithm,

$$m_{mig}(\mathbf{x}) = \int \mathcal{G}(\mathbf{r},\mathbf{s},\mathbf{x},t) \otimes \ddot{d}(\mathbf{r},t|\mathbf{s},0)|_{t=0}\ d\mathbf{r}\ d\mathbf{s}\ dt, \tag{6.1}$$

with the migration kernel defined as

$$\mathcal{G}(\mathbf{r},\mathbf{s},\mathbf{x},t) = g(\mathbf{s},t|\mathbf{x},0) * g(\mathbf{r},t|\mathbf{x},0), \tag{6.2}$$

where $*$ denotes temporal convolution and $\otimes$, together with $t=0$, represents the correlation at zero-lag time (which is equivalent to a dot product in the data coordinates). The $\ddot{d}(\mathbf{r},t|\mathbf{s},0)$ term represents the second time derivative of the trace at the receiver point $\mathbf{r}$ with the source point at $\mathbf{s}$, while the $g(\mathbf{s},t|\mathbf{x},0)$ and $g(\mathbf{r},t|\mathbf{x},0)$ terms represent the scattered Green's functions which, respectively, propagate the energy from the subsurface trial image point $\mathbf{x}$ to the surface source point at $\mathbf{s}$ and the receiver point $\mathbf{r}$. The term $\mathcal{G}(\mathbf{r},\mathbf{s},\mathbf{x},t)$ acts as the migration operator or focusing kernel (Schuster, 2002) which migrates the reflection in $\ddot{d}(\mathbf{r},t|\mathbf{s},0)$ to the trial image point $\mathbf{x}$. It is obtained by a FD solution to the wave equation with a point source $\mathbf{s}$ on the surface and a scattering point at the image point $\mathbf{x}$, and convolving this source-side Green's function $g(\mathbf{s},t|\mathbf{x},0)$ with the receiver-side Green's function $g(\mathbf{r},t|\mathbf{x},0)$.

A simple diagram shown in Figure 6.1 illustrates the difference between the diffraction-stack migration and GDM operators plotted in data-space coordinates. Figure 6.1a shows the traditional migration curve for diffraction-stack migration which is also known as Kirchhoff migration. The usual interpretation is that the migration image at $\mathbf{x}$ is given by summing the trace amplitudes along the hyperbola, i.e., the migration image is the dot

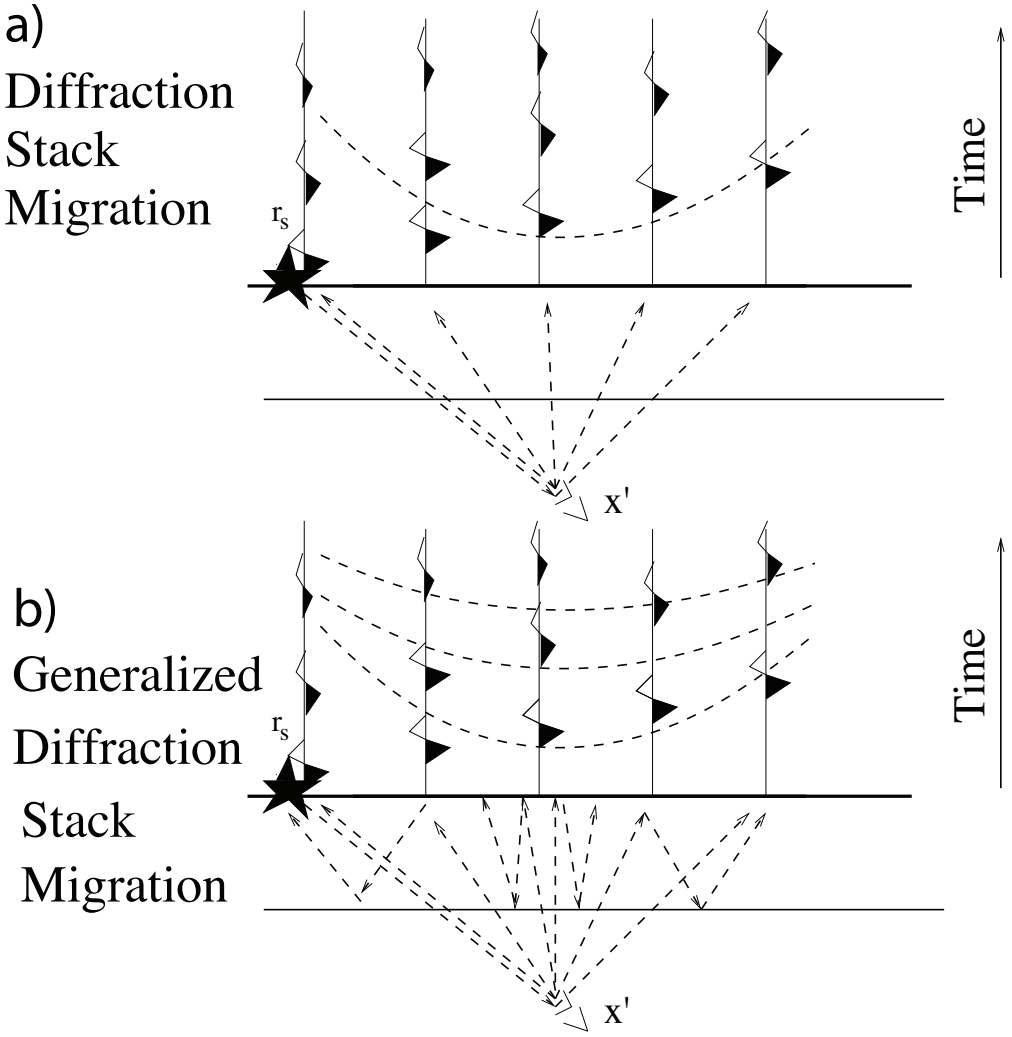

Figure 6.1. Diffraction-stack migration versus generalized diffraction-stack migration. a) Simple diffraction-stack migration operator (dashed hyperbola) and data, which only contains first arrival scattering information. b) Generalized diffraction-stack migration operator (dashed hyperbolas) which contains all events in the migration model, including multiples, diffractions and reflections.

product of the recorded shot gathers with the migration operator (a single hyperbolic curve shown in Figure 6.1a). Figure 6.1b illustrates the idea behind GDM: take the dot product of the recorded shot gathers with the generalized migration operator $\mathcal{G}(\mathbf{r},\mathbf{s},\mathbf{x},t)$. Note that all events are included in the generalized migration operator such as direct waves, multiples, reflections and diffractions as well.

But the major problem with the above approach is that the migration operator $\mathcal{G}(\mathbf{r},\mathbf{s},\mathbf{x},t)$ is a five-dimensional matrix with the dimension size determined by the model size, the number of sources and receivers, and the number of samples within a trace. It means that $\mathcal{G}(\mathbf{r},\mathbf{s},\mathbf{x},t)$ is too expensive to be stored. To reduce the the cost of I/O and storage of the $\mathcal{G}(\mathbf{r},\mathbf{s},\mathbf{x},t)$, I only store the early-arrivals of $g(\mathbf{s},t|\mathbf{x},0)$ followed by skeletonization to reduce the size of the migration kernel by at least two orders-of-magnitude.

The skeletonized least-squares GDM algorithm is as follows:

1. Compute the Green's functions $g(\mathbf{s},t|\mathbf{x},0)$ by a numerical solution to the wave equation for a point source at trial image point $\mathbf{x}$ and recorded at source position $\mathbf{s}$. Since $\mathbf{s}$ occupies the same positions as $\mathbf{r}$, then $g(\mathbf{r},t|\mathbf{x},0)$ is considered the same as $g(\mathbf{s},t|\mathbf{x},0)$.

2. Skeletonize $g(\mathbf{s},t|\mathbf{x},0)$ to $\hat{g}(\mathbf{s},t|\mathbf{x},0)$. Early-arrivals are used and each important early-arrival event is replaced by a single time sample after skeletonization. In this way, a calculated Green's function trace with 501 samples is reduced to a sparse trace with about 25 samples.

3. The skeletonized Green's function $\hat{g}(\mathbf{s},t|\mathbf{x},0)$ is associated with the recording position at $\mathbf{s}$ and $\hat{g}(\mathbf{r},t|\mathbf{x},0)$ is that recorded at $\mathbf{r}$. Those two Green's functions are convolved to generate the migration kernel:

$$\hat{\mathcal{G}}(\mathbf{r},\mathbf{s},\mathbf{x},t) = \hat{g}(\mathbf{s},t|\mathbf{x},0) * \hat{g}(\mathbf{r},t|\mathbf{x},0). \tag{6.3}$$

4. The migration operator $\hat{\mathcal{G}}(\mathbf{r},\mathbf{s},\mathbf{x},t)$ is a Kirchhoff-like kernel that describes, for a single shot gather, pseudo-hyperbolas of multiarrivals in $\mathbf{r}-t$ space. The reflection energy in a recorded shot gather $d(\mathbf{r},t|\mathbf{s},0)$ is then summed along such pseudo-hyperbolas to give the migration image,

$$m_{mig}(\mathbf{x}) = \sum_{\mathbf{s}}\sum_{\mathbf{r}}\sum_{t} \hat{\mathcal{G}}(\mathbf{r},\mathbf{s},\mathbf{x},t)\ d(\mathbf{r},t|\mathbf{s},0). \tag{6.4}$$

5. The above $\hat{\mathcal{G}}(\mathbf{r},\mathbf{s},\mathbf{x},t)$ is used for iterative LSM by a conjugate gradient method.

The advantages of skeletonized least-squares GDM are that 1). the high-frequency approximation of Kirchhoff migration is largely not needed; 2). the storage requirement for the migration kernel is reduced by more than two orders-of-magnitude compared to storing every sample in a calculated migration kernel; 3). these migration operators do not need to be recalculated for each LSM iteration; 4). inclusion of just a few important early-arrival events can significantly reduce artifacts seen in conventional RTM images.

In contrast, the main drawback of skeletonized least-squares GDM is that the choice of important events is somewhat arbitrary and so can lead to missing important information in the migration operator. However, the migration operator is only as accurate as our knowledge of the subsurface velocity model so important events might be just the early-arrivals.

6.3 Numerical Results

The skeletonized least-squares GDM method is tested on synthetic data associated with the 2D SEG/EAGE salt model (see Figure 6.2). These traces were computed by FD solutions to the 2D acoustic wave equation. The data include 162 shot gathers with a peak-frequency of 15 Hz, with 176 traces in each shot gather, the shot and receiver intervals are 97.6 m and 24.4 m, respectively. To save computation time, I down-sampled the traces from 4001 time samples with a time interval of 0.001 to 1001 time samples with a time interval of 0.004 s in each trace.

A simple filtering plus thresholding scheme is used to skeletonize the Green's function. Convolution of the skeletonized traces (early-arrivals windowed with a window length of 5 periods) of both the source-side and the receiver-side Green's functions is computed and the migration kernels are saved to disk.

Figure 6.3a shows the migration of the 2D SEG/EAGE data set using the GDM scheme. The shallow structures are contaminated by the large amplitude artifacts due to the strong reflection at the ocean bottom. Artifacts are also clearly noticeable around the up boundary of the salt at 1.5 km. Figure 6.3b shows the result after applying a low-cut filter. The major part of the artifacts are removed.

A preconditioned conjugate gradient LSM method is then implemented with Figure 6.3a as the starting model. All of the migration kernels are available, so no new simulations are needed to get the updated migration image at each iteration. This is the key point for an efficient implementation of iterative LSM, and the result after 10 iterations is shown in Figure 6.3c. These strong artifacts are successfully eliminated by the least-squares iterations. Compared to Figure 6.3b, the structure below the salt dome and faults are

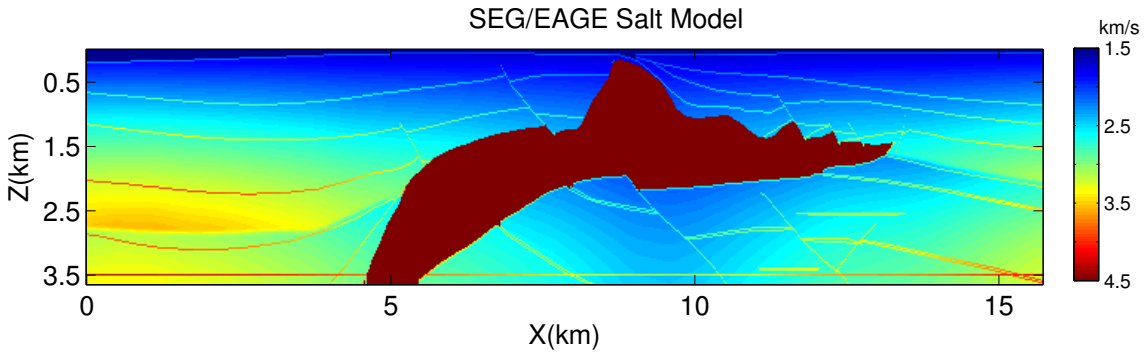

Figure 6.2. The 2D SEG/EAGE velocity model.

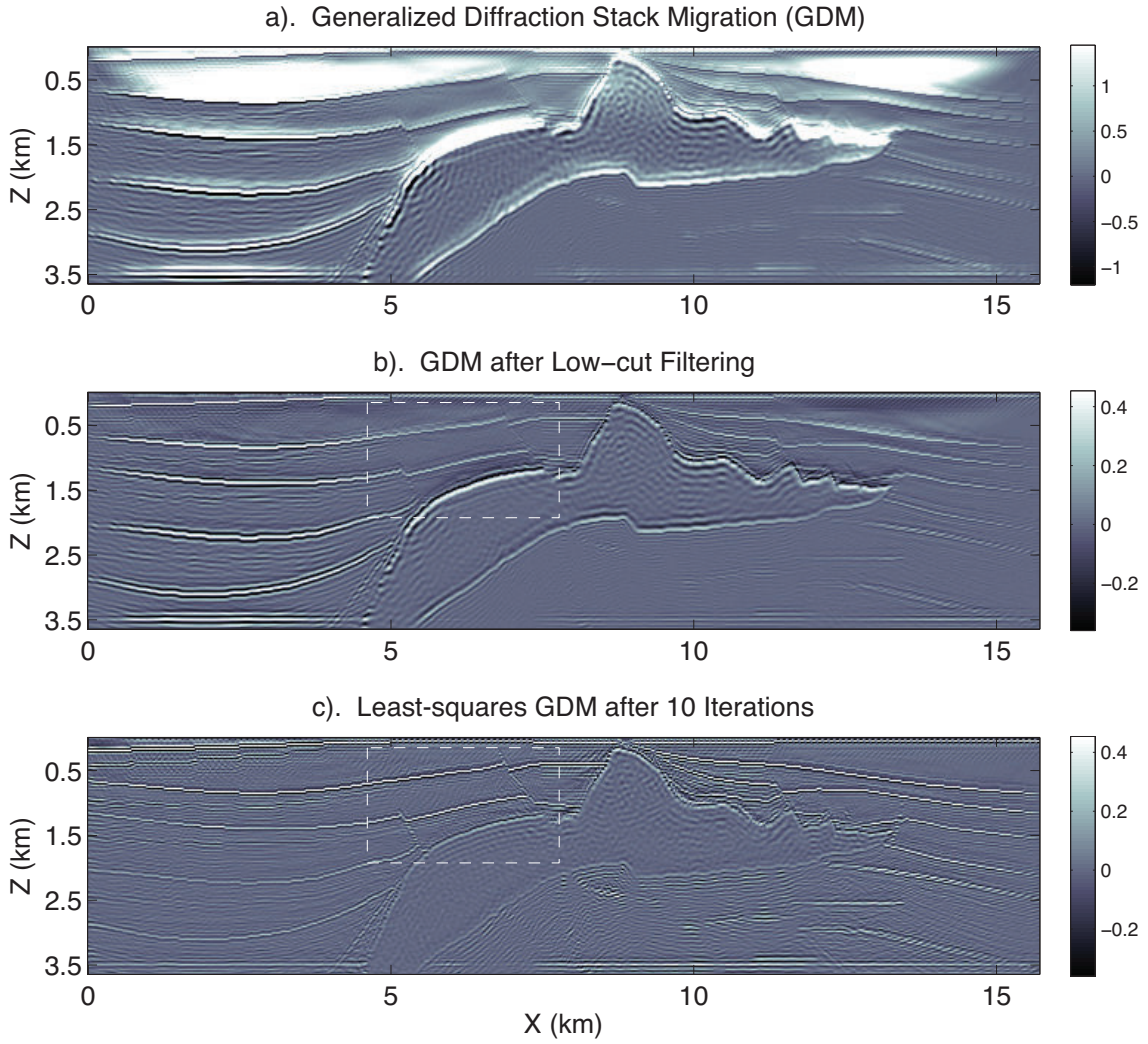

Figure 6.3. Migration results for all 162 shot gathers of the SEG/EAGE salt model: a) GDM result which is identical to standard RTM image; b) low cut filtered version of a); c) skeletonized least-squares GDM image after 10 iterations.

more clearly resolved in Figure 6.3c. This is demonstrated in Figure 6.4, which shows zoom views of Figure 6.3b and Figure 6.3c.

6.4 Summary

The theory for skeletonized least-squares wave equation migration is presented. The key idea is to solve the wave equation only once to get the Green's functions. These Green's functions are skeletonized into a few samples and saved to disk. The skeletonized migration kernel is obtained through convolution of source-side and receiver-side Green's functions followed by a filtering plus thresholding scheme. Both storage and I/O costs are greatly reduced compared to saving the entire migration kernel, and the GDM image is computed by a dot product of the migration operator with the recorded shot gathers. The outstanding feature of skeletonized least-squares GDM is that in the least-squares mode, the migration kernel is reused and does not require new solutions to the wave equation. Hence, least-squares GDM might not be significantly more costly than standard RTM. If this procedure is combined with multisource technology, I believe that the cost of it is much less than that of conventional RTM. This method can also be used with one-way wave equation methods such as phase-shift migration and is applicable for rapid migration velocity analysis as well.

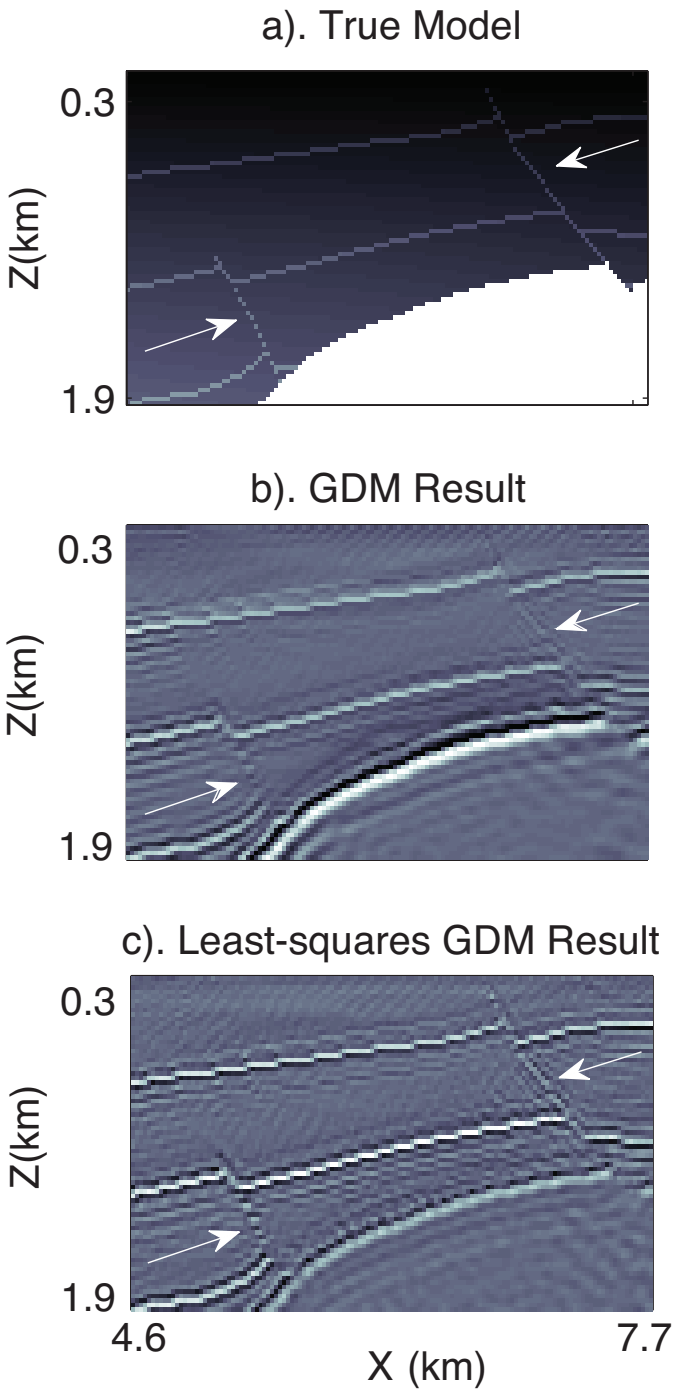

Figure 6.4. Zoom view of the migration results. a) shows the true model, b) and c) are the GDM results before and after least-squares iterations.

CHAPTER 7

PHASE-ENCODED WAVE-EQUATION MIGRATION

The theory for least-squares generalized diffraction-stack migration (LSGDM) was presented in Chapter 6. Now I test the performance of LSGDM using the phase-encoded multisource technology. The key idea is, for an assumed velocity model, the receiver-side Green's function and the source-side Green's function are computed by a numerical solution of the wave equation. The multisource migration operator is formed by convolution of these two Green's functions followed by phase-encoding. Recorded shot gathers are phase-encoded together with the same phase-encoding function to form a supergather. Then the GDM image is obtained by an $x-t$ domain dot product between the supergather and the multisource migration operator for every trial image point. The dot product of unrelated migration operators and shot gathers inevitably brings cross-talk noise into the migration image. To deal with such noise, the least-squares algorithm is adopted. Numerical results show that the LSGDM method combined with the phase-encoded multisource technology can lead to an efficient computation of wave equation least-squares migration (LSM) images in almost the same time as that of conventional reverse-time migration (RTM). It is especially suited to efficient target oriented migration.

7.1 Introduction

Wave equation migration methods can be very expensive compared to diffraction-stack migration methods. The conventional RTM approach requires a numerical solution to the wave equation for every source position. Hence, much research effort has been spent in reducing the costs of RTM.

I propose to reduce the costs of both standard RTM and least-squares RTM by calculating the blended migration operator $\tilde{\Gamma}(\mathbf{r},\mathbf{x}) = \sum_s N(\mathbf{s})G(\mathbf{x}|\mathbf{r})^* G(\mathbf{x}|\mathbf{s})^*$, and then save it on disk. When the blended migration kernel is ready, the migration image can be obtained by a dot product of $\mathcal{F}^{-1}(\tilde{\Gamma})$ and the recorded shot gathers in the $x-t$ domain; here, $\mathcal{F}^{-1}$

denotes the inverse Fourier transform. Because the migration kernels for the whole model space is too large to be saved, I phase-encode the migration kernels as well as phase-encode the recoded shot gathers before doing the dot product. This reduces the memory cost by at least an order-of-magnitude.

Once the blended migration kernel is saved, it does not need to be recomputed at each LSM iteration so this can result in almost two orders-of-magnitude reduction in cost for iterative least-squares migration (Nemeth et al., 1999; Aoki and Schuster, 2009). A further decrease in cost can be achieved by phase-encoding and multisource migration.

In this chapter, I briefly introduce the least-squares phase-encoded GDM theory first, followed by numerical tests on the 2D SEG/EAGE salt model that demonstrate the effectiveness of this method. Conclusions are drawn at the end.

7.2 Theory

Phase-encoded GDM is an alternative to phase-encoded RTM but in a different way. To facilitate an understanding, I first present the theory for phase-encoded RTM, followed by that for phase-encoded GDM. Finally, the theory for least-squares phase-encoded GDM is introduced.

7.2.1 Phase-encoded Reverse-time Migration

The phase-encoded multisource traces are first formed by summing the encoded traces from all mono-frequency shot gathers. Here I assume a fixed spread geometry. Then the phase-encoded RTM method back-projects every multisource trace and migrating with the following formula

$$\begin{aligned} m(\mathbf{x}) &= \sum_r \sum_s G(\mathbf{x}|\mathbf{r})^* \tilde{D}(\mathbf{r}) [N(\mathbf{s}) G(\mathbf{x}|\mathbf{s})]^*, \\ &= \sum_r \overbrace{G(\mathbf{x}|\mathbf{r})^* \tilde{D}(\mathbf{r})}^{back\ propagate} \sum_s \overbrace{[N(\mathbf{s}) G(\mathbf{x}|\mathbf{s})]^*}^{forward\ propagate}, \\ &= B(\mathbf{x}) F(\mathbf{x}), \end{aligned} \tag{7.1}$$

where $\mathbf{x}\ \epsilon\ V$, $B(\mathbf{x}) = \sum_g G(\mathbf{x}|\mathbf{r})^* \tilde{D}(\mathbf{r})$ is the back-projected reflection wavefield and $F(\mathbf{x}) = \sum_s N(\mathbf{s}) G(\mathbf{x}|\mathbf{s})$ is the forward-modeled multisource wavefield at the trial image point $\mathbf{x}$. Also, the *gth* component of the encoded multisource data $\tilde{D}$ is denoted by $\tilde{D}(\mathbf{r}) = \omega^2 \sum_s N(\mathbf{s}) D(\mathbf{r}|\mathbf{s})$, where $D(\mathbf{r}|\mathbf{s})$ represents the recorded single-source shot gather, and $\mathbf{r}$ indicates the receiver position on the surface. The data and migration operators are in the frequency domain at angular frequency ω, and N_i is mapped to the function $N(\mathbf{x}_i)$.

7.2.2 Phase-encoded Generalized Diffraction-stack Migration

Phase-encoded GDM is equivalent to the phase-encoded RTM but is implemented in a different order; i.e.,

$$\begin{aligned} m(\mathbf{x}) &= \sum_r \sum_s G(\mathbf{x}|\mathbf{r})^* \tilde{D}(\mathbf{r}) [N(\mathbf{s}) G(\mathbf{x}|\mathbf{s})]^*, \\ &= \sum_r \Big[\sum_s \overbrace{N(\mathbf{s}) G(\mathbf{x}|\mathbf{r})^* G(\mathbf{x}|\mathbf{s})^*}^{migration\ kernel} \Big] \tilde{D}(\mathbf{r}), \\ &= \sum_r \tilde{\Gamma}(\mathbf{r}, \mathbf{x}) \tilde{D}(\mathbf{r}), \end{aligned} \tag{7.2}$$

where

$$\tilde{\Gamma}(\mathbf{r}, \mathbf{x}) = \sum_s N(\mathbf{s}) G(\mathbf{x}|\mathbf{r})^* G(\mathbf{x}|\mathbf{s})^* \tag{7.3}$$

is the convolution of the receiver-side Green's function and the source-side Green's function followed by phase-encoding. It is also known as the multisource migration operator or multisource focusing kernel (Schuster, 2002).

7.2.3 Least-squares Phase-encoded GDM

The LSM method can be applied to the phase-encoded multisource data by a steepest descent method:

$$\mathbf{m^{(k+1)}} = \mathbf{m^{(k)}} - \alpha \mathbf{L^T} [\mathbf{L m^{(k)}} - \mathbf{d}], \tag{7.4}$$

where α is the step length, $\mathbf{L^T} = \tilde{\mathbf{\Gamma}}$ is the multisource migration operator with the kernel given by equation 7.3. The key idea is to solve the wave equation only once to get the Greens functions. The multisource migration operator is obtained by convolution of the receiver-side Green's function and source-side Green's function followed by phase-encoding and then saved on disk. For each LSM iteration, the saved multisource migration kernels are loaded and zero-lag cross-correlated with the data residuals obtained from the previous iteration.

7.3 Numerical Results

The least-squares phase-encoded GDM method is tested on synthetic data associated with the 2D SEG/EAGE salt model (see Figure 7.1). These traces were computed by FD solutions to the 2D acoustic wave equation. The data include 160 shot gathers with a peak-frequency of 15 Hz, with 176 traces in each shot gather, the shot and receiver intervals are 97.6 m and 24.4 m, respectively. To save computation time, I down-sampled the traces

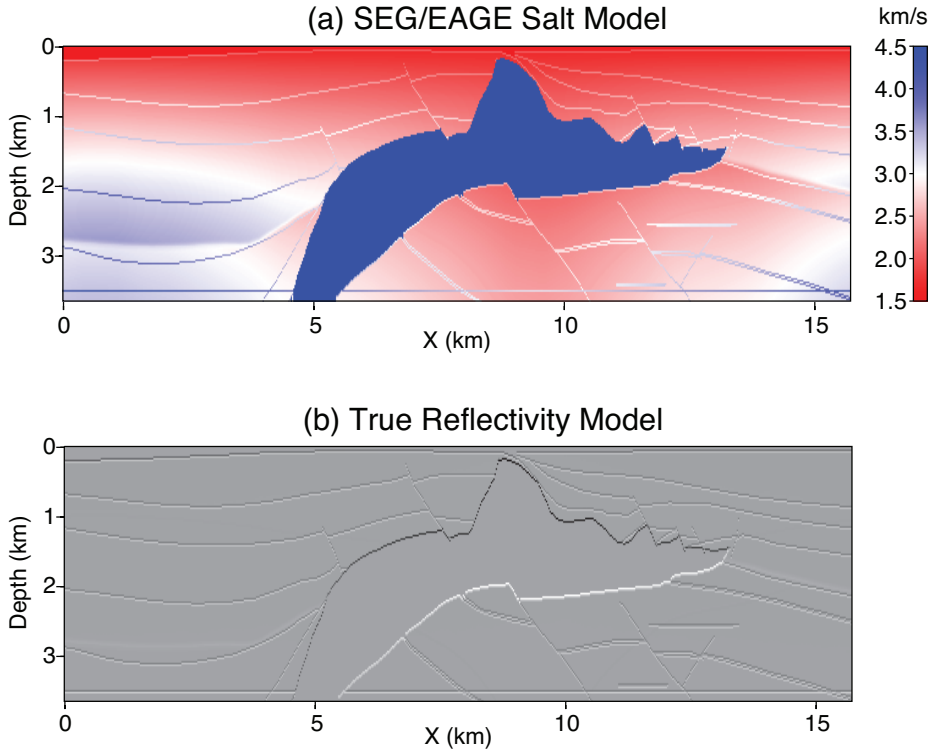

Figure 7.1. The 2D SEG/EAGE velocity model and the corresponding reflectivity model.

from 4001 time samples with a time interval of 0.001 to 1001 time samples with a time interval of 0.004 s in each trace.

For comparison, I implement the single-source GDM first and the results are shown in Figure 7.2 and 7.3. Figure 7.2 shows the first-arrival GDM results, in which the migration kernel is calculated by convolution of the first-arrivals in the source-side Green's function and receiver-side Green's function. In Figure 7.3, the migration kernel is obtained by a full length convolution of two Green's functions. Compared to the LSM image using the full Green's function (Figure 7.3c), the one only using the first-arrival Green's function (Figure 7.2c) looks more noisy and less resolved below the salt body; however, it is much cheaper due to fewer samples in the Green's function for convolution.

Before applying the least-squares method, I did some tests on different phase-encoding functions. There were three types of phase-encoding functions, source statics, receiver statics and random polarity. Figure 7.4 shows such a supergather with different phase-encoding functions.

Figure 7.5 shows the 10-fold multisource GDM results using the first-arrival Green's function and the full Green's function. Only source statics are applied while generating phase-encoded gathers. It is obvious that the shorter duration of the source-side Green's function, the less cross-talk contamination in the migration image.

Figures 7.6 and 7.7 demonstrate the effectiveness of the other two phase-encoding functions, receiver statics and random polarity. From the comparisons of without and with these phase-encoding functions, I can conclude that both of them are valid ways to reduce the cross-talk noise in the migration image. If I combine the source statics together with these two phase-encoding functions, the cross-talk noise in the migration image will be further reduced.

A preconditioned conjugate gradient LSM method is then implemented with Figure 7.8a as the starting model. All of the multisource migration kernels are available, so no new simulations are needed to get the updated migration image at each iteration. This is the key point for an efficient implementation of iterative LSM, and the result after 20 iterations is shown in Figure 7.8b. I note that the low-frequency migration artifacts shown above the salt are successfully eliminated by the least-squares iterations, while faults and small structures below the salt dome are better resolved in Figure 7.8b. The multisource least-squares GDM image (Figure 7.8b) is comparable with the single-source version (Figure 7.8c) but with less random noise; however, the storage cost for the migration kernel and the corresponding I/O cost of it is about 1/10 of the single-source version.

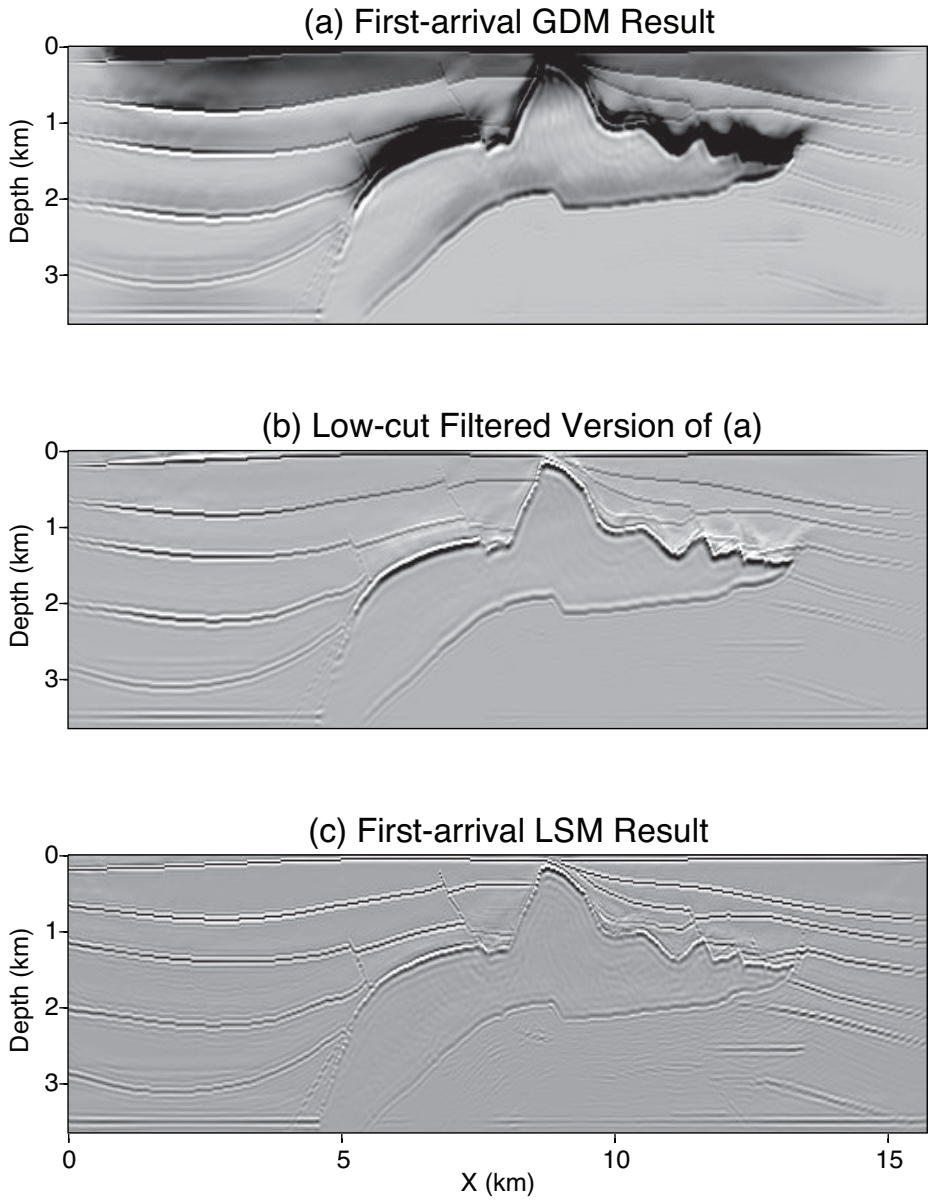

Figure 7.2. Comparison of single-source GDM results using the first-arrival Green's function.

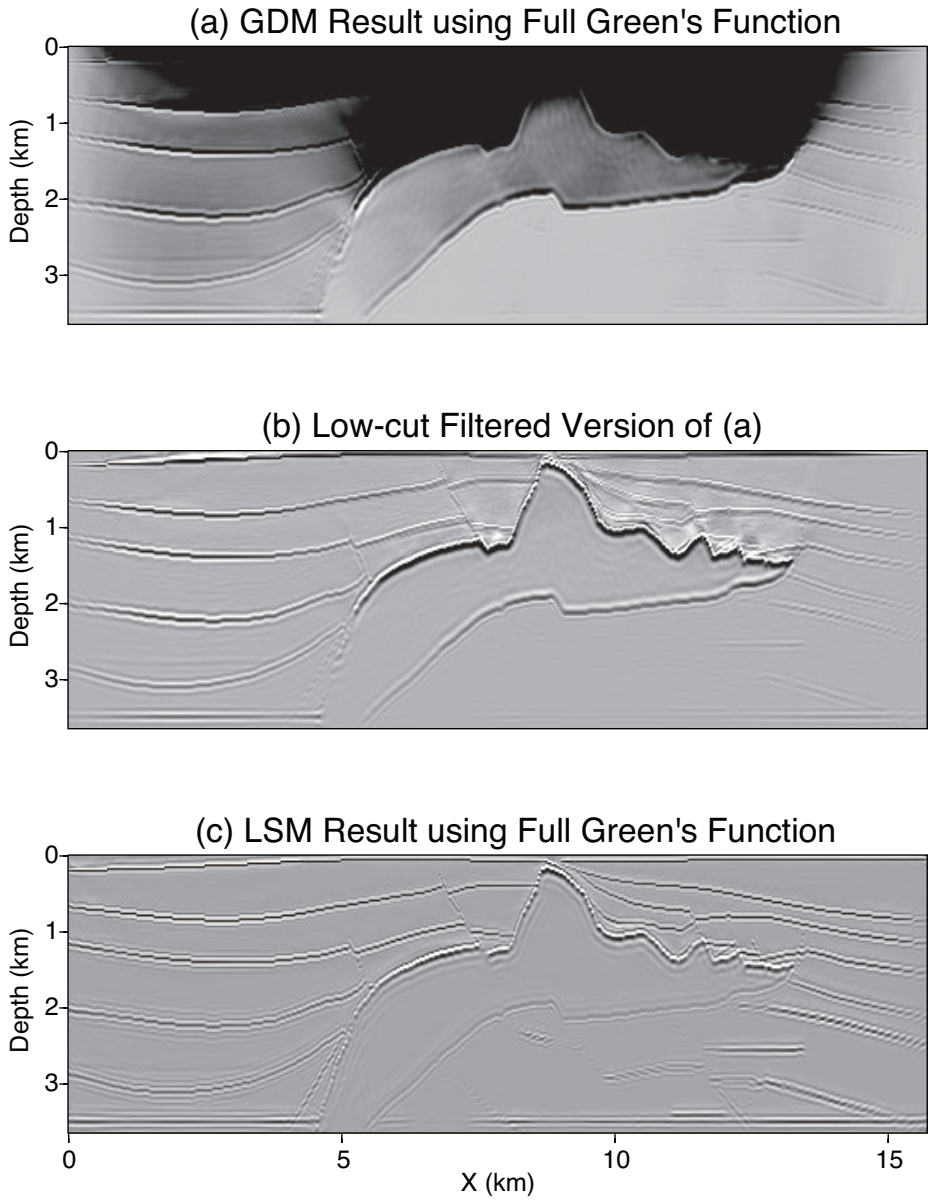

Figure 7.3. Comparison of single-source GDM results using the full Green's function.

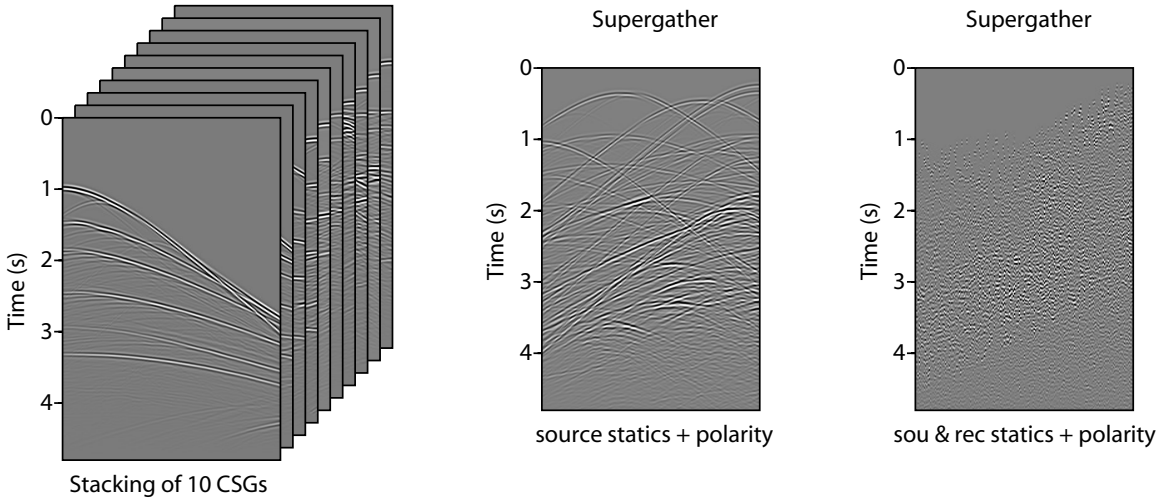

Figure 7.4. Formation of phase-encoded supergathers with different phase-encoding functions.

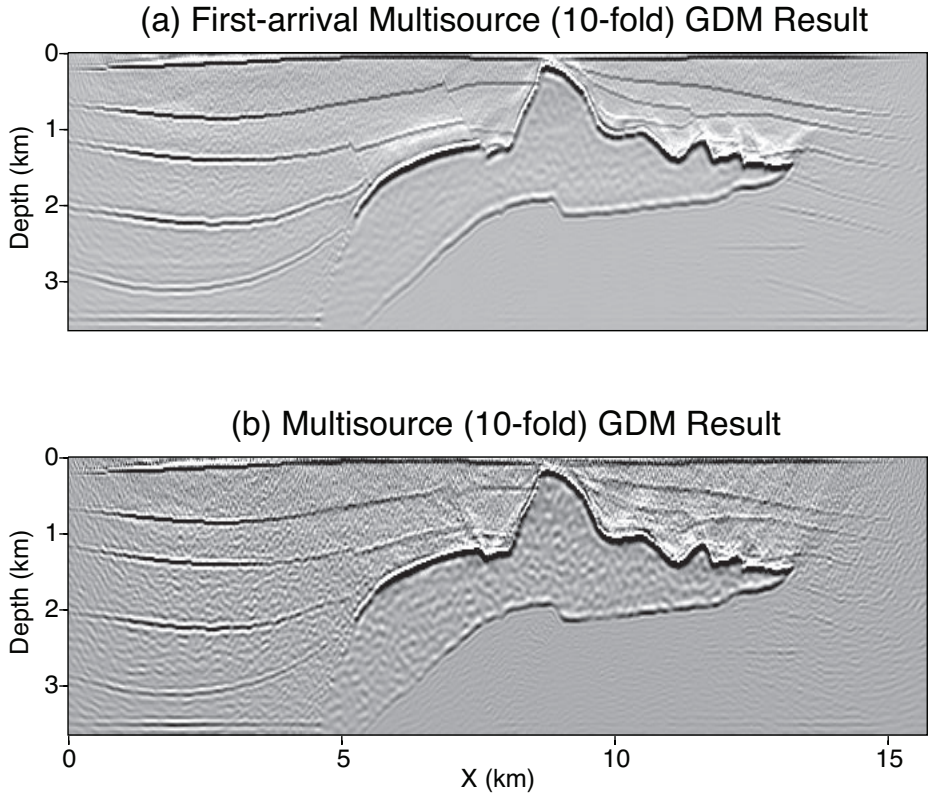

Figure 7.5. Comparison of multisource GDM results without iterations using the first-arrival Green's function and the full Green's function. Ten shot gathers are phase-encoded in a supergather using source statics phase-encoding.

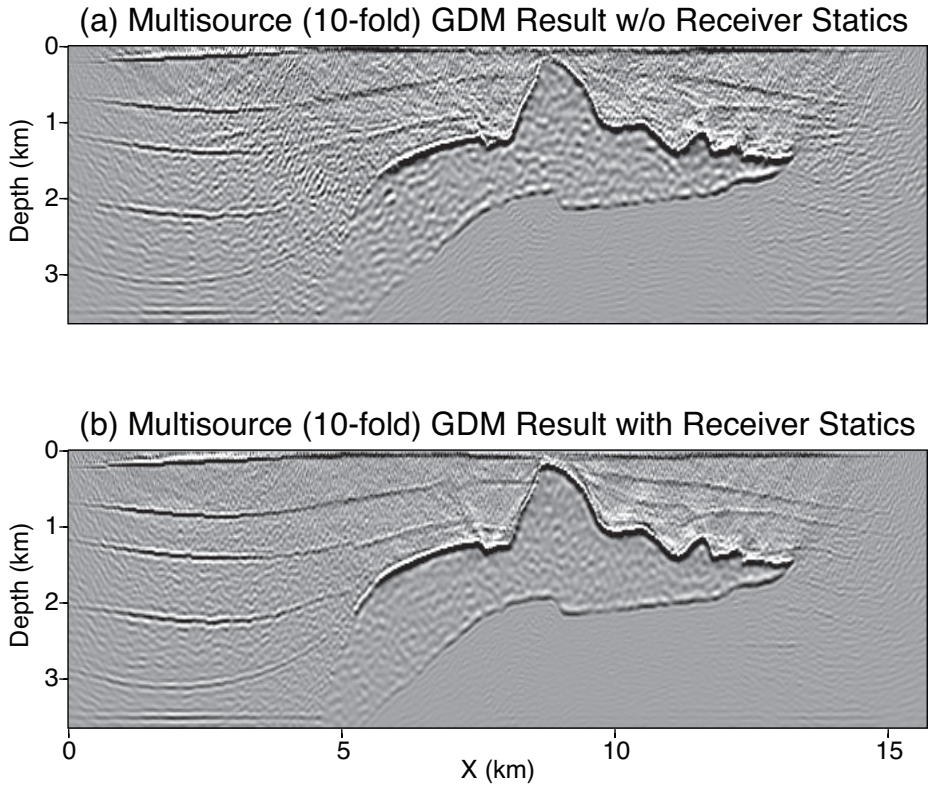

Figure 7.6. Comparison of multisource GDM results without and with applying receiver statics.

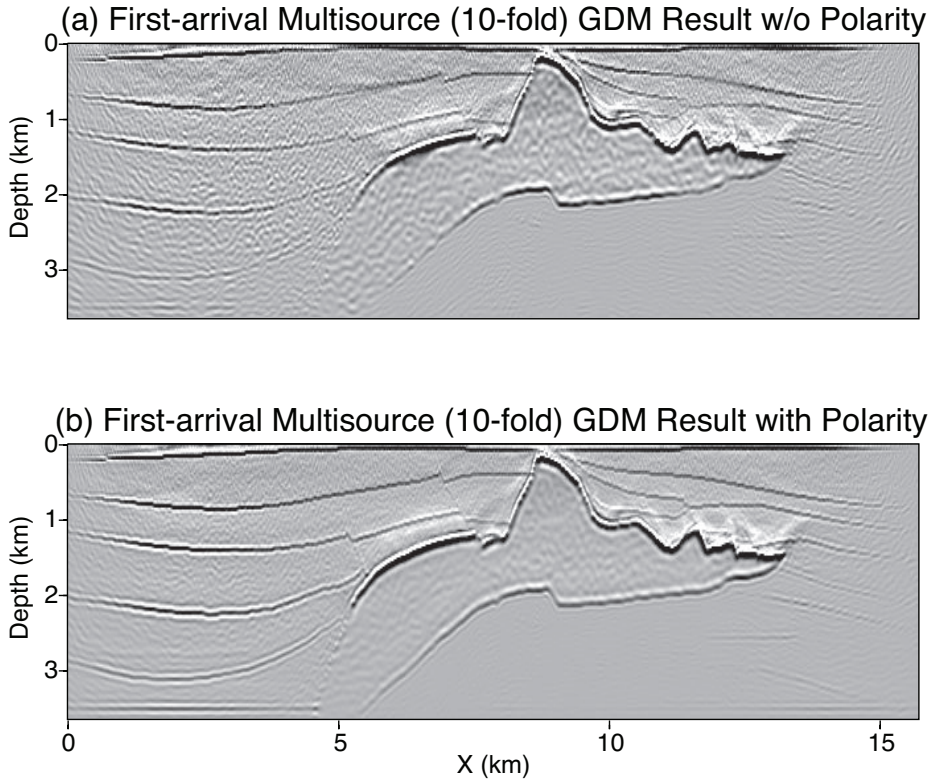

Figure 7.7. Comparison of multisource GDM results without and with applying random polarity.

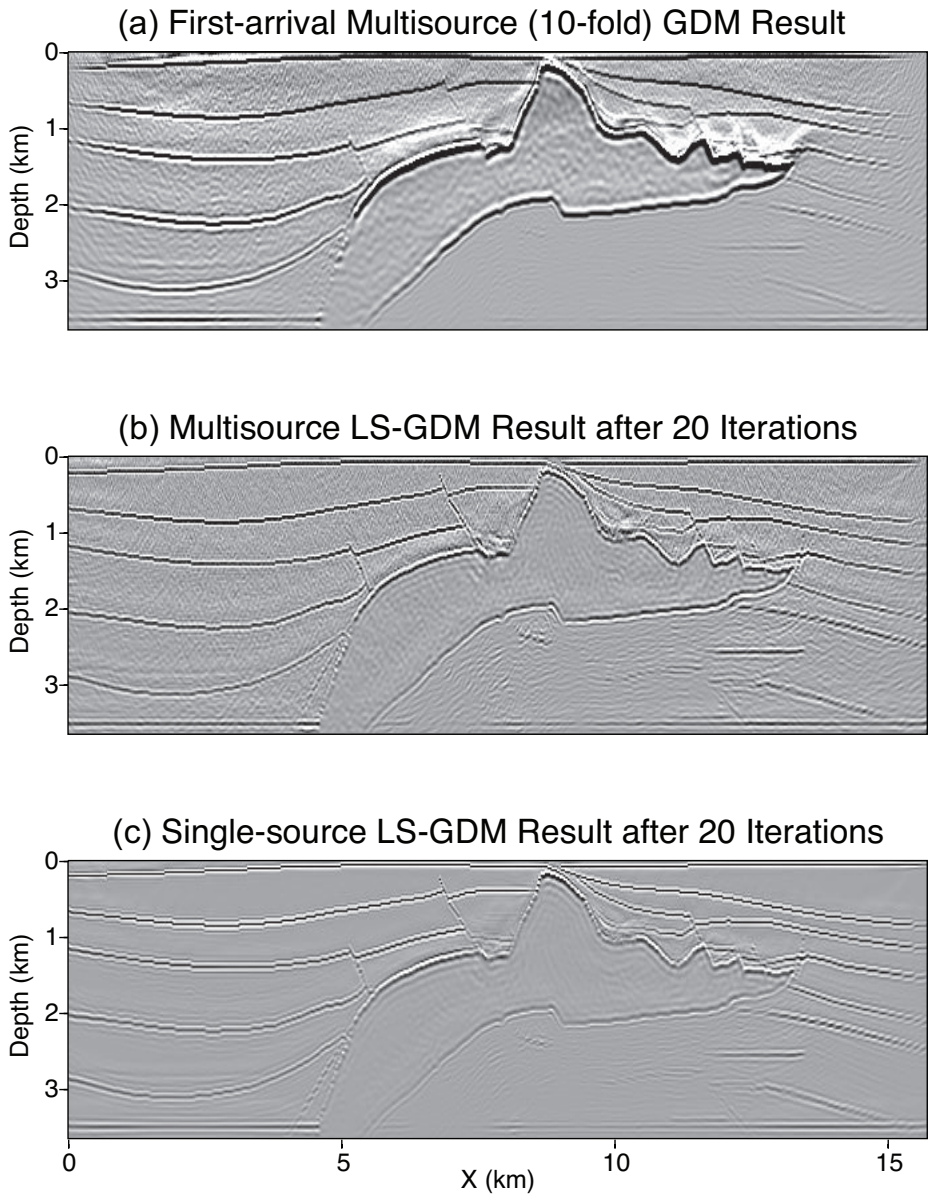

Figure 7.8. The least-squares phase-encoded GDM image after 20 iterations(b) with the starting model of (a). (c) is the least-squares GDM image after 20 iterations without phase-encoding which is 10 times slower than (b). Source and receiver statics and random polarity are all employed in this test.

7.4 Summary

The theory for least-squares phase-encoded GDM is presented. The key idea is to solve the wave equation only once to get the receiver-side Green's function and the source-side Green's function. The multisource migration kernel is obtained through convolution of the receiver-side Green's function and the source-side Green's function followed by phase-encoding. Both storage and I/O costs of migration kernel are greatly reduced due to phase-encoding, and the multisource GDM image is computed by a dot product of the multisource migration kernel with the phase-encoded shot gathers. The outstanding feature of least-squares phase-encoded GDM is that the multisource migration kernel is reused at each iteration and does not require new solutions to the wave equation. Hence, least-squares phase-encoded GDM might not be significantly more costly than standard RTM.

However, there are some limitations with GDM compared to RTM. Even with a phase-encoding scheme, the size of the multisource migration kernel is still a function of number of receivers, number of time samples and the computational model size. In the 2D case, it takes hundreds of gigabytes of storage, and loading all of the migration kernels at each iteration is time consuming. For 3D, the storage cost of the migration kernel will be many times more than the 2D case. Therefore this method is not ready for use with 3D surveys except in a target oriented mode. Future work will be focused on further compression of the multisource migration kernel and multisource cross-talk noise elimination.

APPENDIX A

COMPUTATION OF THE MIGRATION KERNEL

The migration kernel in equation 2.5 can be computed in one of two ways.

1. Place a source point on the surface at $\mathbf{s}$, and solve for the field everywhere in the model by a finite-difference method to get the Green's function $g(\mathbf{x}, t|\mathbf{s}, 0)$. Reciprocity says that $g(\mathbf{s}, t|\mathbf{x}, 0) = g(\mathbf{x}, t|\mathbf{s}, 0)$, and if we replace $\mathbf{s} \rightarrow \mathbf{r}$ then this gives $g(\mathbf{r}, t|\mathbf{x}, 0)$. Thus, $g(\mathbf{r}, t|\mathbf{x}, 0)$ can be convolved with $g(\mathbf{x}, t|\mathbf{s}, 0)$ to give the migration kernel $\mathcal{G}(\mathbf{r}, \mathbf{s}, \mathbf{x}, t)$ in equation 2.5 with the receiver at $\mathbf{r}$ and the source at $\mathbf{s}$ for all subsurface points $\mathbf{x}$.

2. Alternatively, a point source can be placed at depth $\mathbf{x}$ and the field can be solved everywhere to get $g(\mathbf{r}, t|\mathbf{x}, 0)$. This can be cost effective for target-oriented migration (or waveform inversion) so that we only need the Green's functions for point sources along the boundary of the target (Dong et al., 2009). Reciprocity says that $g(\mathbf{r}, t|\mathbf{x}, 0) = g(\mathbf{x}, t|\mathbf{r}, 0)$, and letting $\mathbf{r} \rightarrow \mathbf{s}$ yields $g(\mathbf{x}, t|\mathbf{s}, 0)$. The migration kernel at $\mathbf{x}$ can now be computed by equation 2.5. This is the method used by Liu and Wang (2008) and Dong et al. (2009) for target-oriented migration.

Zhou and Schuster (2002) demonstrated how to efficiently compute these migration operators by finite differencing along the leading portion of the wavefront.

APPENDIX B

COMPRESSION OF THE MIGRATION KERNEL

A wavelet transform with compression (Zhan and Schuster, 2010) can be used to reduce storage costs associated with the the GDM kernel, as follows.

1. Compute the source-side $g(\mathbf{x},t|\mathbf{s},0)$ and the receiver-side $g(\mathbf{x},t|\mathbf{r},0)$ bandlimited Green's functions by a numerical solution to the wave equation.

2. A wavelet transform (Luo and Schuster, 1992) is applied to the Green's function $g(\mathbf{x},t|\mathbf{s},0)$ and $g(\mathbf{x},t|\mathbf{r},0)$ to get $\mathcal{W}[g(\mathbf{x},t|\mathbf{s},0)]$ and $\mathcal{W}[g(\mathbf{x},t|\mathbf{r},0)]$, respectively. Here, $\mathcal{W}$ represents the wavelet transform with up to an order-of-magnitude reduction in storage requirements (Luo and Schuster, 1992). Then, mute all wavelet coefficients below a given threshold in the wavelet domain and only store the significant coefficients to get the compressed Green's functions $\mathcal{W}[\tilde{g}(\mathbf{x},t|\mathbf{s},0)]$ and $\mathcal{W}[\tilde{g}(\mathbf{x},t|\mathbf{r},0)]$. Save these compressed Green's functions on the disk.

3. After reading these compressed Green's functions from disk, an inverse wavelet transform is performed to reconstruct the Green's functions $\tilde{g}(\mathbf{x},t|\mathbf{s},0)$ and $\tilde{g}(\mathbf{x},t|\mathbf{r},0)$ by decompressing $\mathcal{W}[\tilde{g}(\mathbf{x},t|\mathbf{s},0)]$ and $\mathcal{W}[\tilde{g}(\mathbf{x},t|\mathbf{r},0)]$. This is followed by a convolution step using a FFT to get the compressed migration kernel $\tilde{\mathcal{G}}(\mathbf{r},\mathbf{s},\mathbf{x},t)$ in equation 2.5:

$$\tilde{\mathcal{G}}(\mathbf{r},\mathbf{s},\mathbf{x},t) \;=\; \tilde{g}(\mathbf{x},t|\mathbf{s},0) * \tilde{g}(\mathbf{x},t|\mathbf{r},0), \tag{B.1}$$

   where $\tilde{g}(\mathbf{x},t|\mathbf{r},0) = \mathcal{W}^{-1}[\tilde{g}(\mathbf{x},t|\mathbf{r},0)]$. Here, tilde denotes the function after lossy compression and decompression.

4. The compressed migration operator $\tilde{\mathcal{G}}(\mathbf{r},\mathbf{s},\mathbf{x},t)$ is a Kirchhoff-like kernel that describes, for a single shot gather, pseudo-hyperbolas of multiarrivals in $\mathbf{r}$-t coordinates.

The reflection energy in a recorded shot gather $d(\mathbf{r}, t|\mathbf{s}, 0)$ is then summed along such pseudo-hyperbolas to give the migration image,

$$m_{mig}(\mathbf{x}) \quad = \quad \sum_s \sum_r \sum_t \tilde{\mathcal{G}}(\mathbf{r}, \mathbf{s}, \mathbf{x}, t) d(\mathbf{r}, t|\mathbf{s}, 0). \tag{B.2}$$

This summation is equivalent to a dot product between the recorded shot gathers and the compressed GDM kernels, and has the advantage over Kirchhoff migration in that there is no high-frequency approximation and multiarrivals are included in the imaging.

REFERENCES

[1] Abma, R., Sun, J., and Bernitsas, N., 1999, Antialiasing methods in Kirchhoff migration: *Geophysics*, **64**, 1783–1792.

[2] Aoki, N., and Schuster, G. T., 2009, Fast least-squares migration with a deblurring filter: *Geophysics*, **74**, WCA83–WCA93.

[3] Biondi, B., 2001, Kirchhoff imaging beyond aliasing: *Geophysics*, **66**, 654–666.

[4] Blomgren, P., Papanicolaou, G., and Zhao, H., 2002, Super-resolution in time-reversal acoustics: *J. Acoust. Soc. Am.*, **111**(1), 230–248.

[5] Cao, W., 2007, Wave-equation wavefront migration: *SEG Expanded Abstracts*, **26**, 2155–2159.

[6] Claerbout, J., 1992, Earth Soundings Analysis: Processing versus Inversion: *Blackwell Science Ltd.*, London, UK.

[7] Dai, W., and Schuster, G. T., 2009, Least-squares migration of simultaneous sources data with a deblurring filter: *SEG Expanded Abstracts*, **28**, 2990–2994.

[8] Dai, W., Fowler, P., and Schuster, G. T., 2012, Multi-source least-squares reverse time migration: *Geophysical Prospecting*, **60**, 681–695.

[9] Dong, S., Luo, Y., Xiao, X., Chavez-Perez, S., and Schuster, G. T., 2009, Fast 3D target-oriented reverse time datuming: *Geophysics*, **74**, 141–151.

[10] Dragoset, B., 1999, A practical approach to surface multiple attenuation: *The Leading Edge*, **18**, 104–108.

[11] Elmore, W., and Heald, M., 1969, Physics of waves: *Dover Publications*, New York.

[12] Fei, T., Luo, Y., and Schuster, G. T., 2010, De-blending reverse time migration: *SEG Expanded Abstracts*, **29**, 3130–3134.

[13] Fletcher, R. F., Fowler, P., Kitchenside, P., and Albertin, U., 2005, Suppressing artifacts in prestack reverse time migration: *SEG Expanded Abstracts*, **24**, 2049–2051.

[14] French, W., 1974, Two-dimensional and three-dimensional migration of model-experiment reflection profiles: *Geophysics*, **39**, 265–277.

[15] Gray, S. H., 1992, Frequency-selective design of the Kirchhoff migration operator: *Geophysical Prospecting*, **40**, 565–571.

[16] Guitton, A., Kaelin, B., and Biondi, B., 2006, Least-square attenuation of reverse time migration artifacts: *SEG Expanded Abstracts*, **25**, 2348–2352.

[17] Hanafy, S., Cao, W., McCarter, K., and Schuster, G. T., 2009, Using super-stacking and super-resolution properties of time-reverse mirrors to locate trapped miners: *The Leading Edge*, **28**, 302–307.

[18] Krebs, J. R., Anderson, J. E., Hinkley, D., Neelamani, R., Lee, S., Baumstein, A., and Lacasse, M.-D., 2009, Fast full-wavefield seismic inversion using encoded sources: *Geophysics*, **74**, WCC177–WCC188.

[19] Lerosey, G., Rosny, J. de, Tourin, A., and Fink, M., 2007, Focusing beyond the diffraction limit with far-field time reversal: *Science*, **315**, 1120–1122.

[20] Liu, F., Zhang G., Morton, S., and Leveille, J., 2007, Reverse-time migration using one-way wavefield imaging condition: *SEG Expanded Abstracts*, 2170-2174.

[21] Liu, W., and Wang, Y., 2008, Target-oriented reverse time migration for two-way prestack depth imaging: *SEG Expanded Abstracts*, **27**, 2326–2330.

[22] Liu, F., Zhang, G., Morton S., and Leveille, J., 2011, An effective imaging condition for reverse time migration using wavefield decomposition: *Geophysics*, **76**, S29–S39.

[23] Loewenthal, D., Stoffa, P., and Faria, E., 1987, Suppressing the unwanted reflections of the full wave equations: *Geophysics*, **52**, 1007–1012.

[24] Lumley, D. E., Claerbout, J., and Bevc D., 1994, Anti-aliased Kirchhoff 3-D migration: *SEG Expanded Abstracts*, **13**, 1282–1285.

[25] Luo, Y., and Schuster, G. T., 1992, Wave packet transform and data compression: *SEG Expanded Abstracts*, **11**, 1187–1190.

[26] McMechan, G., 1983, Migration by extrapolation of time-dependent boundary values: *Geophysical Prospecting*, **31**, 413–420.

[27] Mora, P., 1989, Inversion = migration + tomography: *Geophysics*, **54**, 1575–1586.

[28] Mulder, W., and Plessix, R., 2003, One-way and two-way wave-equation migration: *SEG Expanded Abstracts*, **22**, 881–884.

[29] Nemeth, T., Wu, C., and Schuster, G. T., 1999, Least-squares migration of incomplete reflection data: *Geophysics*, **64**, 208–221.

[30] Schuster, G. T., 2002, Reverse-time migration = generalized diffraction stack migration: *SEG Expanded Abstracts*, **21**, 1280–1283.

[31] Stolt, R., and Benson, A., 1986, Seismic migration: theory and practice: in *Handbook of Geophysical Exploration*, Volume **5**, *Geophysical Press*, London, UK.

[32] Whitmore, D., 1983, Iterative depth migration by backward time propagation: *SEG Expanded Abstracts*, **2**, 382–385.

[33] Woodward, M., 1992, Wave-equation tomography: *Geophysics*, **57**, 15–26.

[34] Yoon, K., Marfurt, K. J., and Starr, W., 2004, Challenges in reverse time migration: *SEG Expanded Abstracts*, **23**, 1057–1060.

[35] Yoon, K., and Marfurt, K. J., 2006, Reverse time migration using the Poynting vector: *Exploration Geophysics*, **37**, 102–107.

[36] Yu, J., Hu, J., Schuster, G. T., and Estill, R., 2006, Prestack migration deconvolution: *Geophysics*, **71**, S53–S62.

[37] Zhan, G., Luo Y., and Schuster, G. T., 2010, Modified form of reverse time migration tuned to multiples: *EAGE Expanded Abstracts*, P594.

[38] Zhan, G., and Schuster, G. T., 2011, Skeletonized least-squares wave-equation migration: *SEG Expanded Abstracts*, **29**, 3380–3384.

[39] Zhan, G., and Schuster, G. T., 2012, Anti-aliasing filter for reverse-time migration: *EAGE Expanded Abstracts*, P273.

[40] Zhang, Y., Sun, J., and Gray, S., 2003, Aliasing in wavefield extrapolation prestack migration: *Geophysics*, **68**, 629–633.

[41] Zhou, M., and Schuster, G. T., 2002, Wave-equation wavefront migration: *SEG Expanded Abstracts*, **21**, 1292–1296.

[42] Zhou, M., Sun, H., and Schuster, G. T., 2003, The application of primary-only imaging condition to SMAART data: *SEG Expanded Abstracts*, **22**, 1012–1015.

[43] Zhou, M., 2004, POIC-radon filtering of near-offset multiples: *SEG Expanded Abstracts*, **23**, 1317–1320.